THE PENNSYLVANIA STATE UNIVERSITY
SCHREYER HONORS COLLEGE

DEPARTMENT OF MECHANICAL AND NUCLEAR ENGINEERING

NATURAL DYNAMICS OF A PRECESSING VORTEX CORE IN SWIRLING FLOWS

MARK DANIEL FREDERICK
SPRING 2018

A thesis
submitted in partial fulfillment
of the requirements
for a baccalaureate degree
in Mechanical Engineering
with honors in Mechanical Engineering

Reviewed and approved* by the following:

Jacqueline O'Connor
Assistant Professor of Mechanical Engineering
Thesis Supervisor and Honors Adviser

Stephen Lynch
Shuman Family Early Career Professor
Assistant Professor of Mechanical Engineering
Faculty Reader

* Signatures are on file in the Schreyer Honors College.

ABSTRACT

Combustion instability, or the coupling between flame heat release rate oscillations and combustor acoustics, is a significant issue in the operation of gas turbine combustors. This coupling is often driven by oscillations in the flow field. Shear layer roll-up, in particular, has been shown to drive longitudinal combustion instability in multiple systems, including both laboratory and industrial combustors. One method for suppressing combustion instability in these engines would be to suppress the receptivity of the shear layer to acoustic oscillations, severing the coupling mechanism between the acoustics and the flame. Previous work suggested that the existence of a precessing vortex core (PVC) may suppress the receptivity of the shear layer. The goal of this study is to first, understand the basic behavior of a PVC within a flow field, second, confirm that shear layer receptivity suppression is occurring, and lastly, understand the mechanism by which the PVC suppresses the shear layer receptivity. In this work, we couple experiment with linear stability analysis to determine whether a PVC can suppress shear layer receptivity to longitudinal acoustic forcing in a non-reacting swirling flow at a variety of swirl numbers. The shear layer response to the longitudinal acoustic forcing manifests as an $m=0$ mode since the acoustic field is axisymmetric. The PVC has been shown both in experiment and linear stability analysis to have $m=1$ and $m=-1$ modal content. By comparing the relative magnitude of the $m=0$ and $m=-1, 1$ modes, we quantify the impact that the PVC has on the shear layer response. The mechanism for shear layer response is determined using companion forced response analysis, where the shear layer disturbance growth rates mirror the experimental results. Differences in shear layer thickness and azimuthal velocity profiles drive the suppression of the shear layer receptivity to acoustic forcing.

TABLE OF CONTENTS

LIST OF FIGURES v

LIST OF TABLES vii

ACKNOWLEDGEMENTS viii

Chapter 1 Motivation: Gas Turbine Combustion Instability 1

Chapter 2 Literature Review 3

- Importance of Swirl in Combustion Applications 4
- Structure of Swirling Flow 5
- Forcing in Swirling Jets 7
- Precessing Vortex Cores in Swirling Flows 8
- Research Goal 14

Chapter 3 Experimental Facility 15

- Design Overview 15
- Experimental Rig Design 16
- Acoustic Forcing 19
- Diagnostics 19
  - Frequency Analysis 19
  - Particle Image Velocimetry 22
- Data Analysis 25
  - Proper Orthogonal Decomposition 25
  - Azimuthal Decomposition 25
  - Theoretical Formulation 27

Chapter 4 Acoustic Characterization 29

Chapter 5 Precessing Vortex Core Characterization 33

- Swirl Number Clarification 33
- Frequency Characteristics of the PVC 34
- Base Flow Variation with Swirl Number 37
- Self-Excited Dynamics of the Flow 39

Chapter 6 Flow Field Response to Acoustic Forcing 45

- PVC Frequency Response to Acoustic Forcing 45
- Modal Dynamics of Flow Field Response to Acoustic Forcing 48
- Response Suppression Mechanism 53

Chapter 7 Conclusions and Future Work.....57

BIBLIOGRAPHY.....59

LIST OF FIGURES

Figure 1: Combustion instability feedback cycle....3

Figure 2: Typical radial entry swirler configuration [9]....5

Figure 3: An axial cut of a flow undergoing vortex breakdown [8]....6

Figure 4: Stable vortex breakdown with formation of shear layers [11]....6

Figure 5: Temporal progression of vortex breakdown oscillations. Low forcing frequency (top), high forcing frequency (bottom) [14]....8

Figure 6: PVC visualization in a reacting flow [15]....9

Figure 7: Characteristic spatial mode identifying a PVC [16]....10

Figure 8: 3-D Flow Field Visualization of the PVC or global mode *m=1* [16]....10

Figure 9: Self-excited motions of jet deformation (*m=-2)* and coherent structures *(m=-1)* due to the presence of a PVC [19]....12

Figure 10: Mode numbers of characteristic disturbance field in swirling flows....13

Figure 11: Spatial mode energy distribution at three radii of a flow field containing a PVC [19]....14

Figure 12: Swirling test rig....16

Figure 13: Swirler....17

Figure 14: Airfoil inside swirler....18

Figure 15: Laser sheet, shown in green, oriented in the *r-θ* plane (a) and the *r-x* plane (b)..22

Figure 16: Parabolic mirror set up to take data in the *r-θ* plane....23

Figure 17: Interpolated points in cylindrical coordinates (white dots) on velocity magnitude in the *r-θ* plane....26

Figure 18: Acoustic characterization of rig at 65°....30

Figure 19: Acoustic characterization of rig at 55°....32

Figure 20: Acoustic response of the PVC at various flow rates and swirl numbers....35

Figure 21: The response of S=1.43 swirling flows as a fucntion of Strouhal number and bulk flow velocity 37

Figure 22: Variation of time-averaged flow field (base flow) with swirl number in *r-x* (top) and *r-θ* (bottom) planes 39

Figure 23: Energies of POD modes 1-20 for all swirl numbers 40

Figure 24: POD reconstruction and frequency spectrum of swirl numbers that cause a PVC to be formed 41

Figure 25: Strength of PVC modes *m=1* and *m=-1* for three swirl number as a function of radius 42

Figure 26: Distribution of modes at the PVC frequency for three swirl numbers and *r/D=0.7* 44

Figure 27: PVC amplitude response to acoustic forcing at various flow rates and S=1.43 45

Figure 28: Forcing frequency and amplitude sweep at 46.57 m/s and S=0.95 47

Figure 29: Strength of the m=0 mode for a range of swirl numbers at the forcing frequency, 600 Hz 49

Figure 30: Distribution of modes at 600 Hz for six swirl number and *r/D=0.5* (a) and distribution of modes at 600 Hz and the PVC frequency for the three highest swirl numbers and *r/D=0.5* (b) 50

Figure 31: Strength of the m=0 mode for S=0.38 and S=1.43 at a range of forcing frequencies 51

Figure 32: Response of flow at swirl number of S=0.38 to acoustic forcing as seen by pressure transducer and POD modes at various forcing frequencies. Forcing at 400 Hz (a), 500 Hz (b), 600 Hz (c), and 700 Hz (d) 52

Figure 33: Response of flow at swirl number of S=1.43 to acoustic forcing as seen by PT and POD modes at various forcing frequencies. Forcing at 400 Hz (a), 500 Hz (b), 600 Hz (c), and 700 Hz (d) 53

Figure 34: Spatial amplification of flow response to forcing at 700 Hz 54

Figure 35: Variation in peak spatial amplification as a function of non-dimensional forcing frequency for various swirl numbers 55

Figure 36: Radial profiles at various swirl numbers, S, of time-averaged base flow velocity components (a) $\overline{U}_x$ and (b) $\overline{U}_\theta$, at *x/D=0.3* 56

LIST OF TABLES

Table 1: Test matrix with flow state and PVC frequencies 38

ACKNOWLEDGEMENTS

This thesis could have not been completed by myself alone. There are many people who I would like to acknowledge for their help and support along the way. I began this work two and a half years ago when I started working in Dr. O'Connor's Reacting Flow Dynamics Lab. Since then, the research I have done has defined my college career. Dr. O'Connor has patiently supported me the entire time and given me the freedom to make the swirling flow's experiment my own. She has gone beyond the role of an Honor Adviser and it is because of her that I have been able to map my career path and continue onto graduate school.

I want to thank the graduate students who worked in the lab with me, Wyatt Culler, Ankit Tyagi, and Anand Makwana. They were always willing to help and sometimes took hours out of their day to do so. I also need to thank Dr. Steve Peluso, who keeps Research East running and went out of his way to help me. I want to thank Brian Brubaker and Josh Dudash for working with me to collect data. I finally need to thank Sean Clees and Danielle Mason, my fellow undergraduates on this project.

The Schreyer Honors College set me on the path of undergraduate research and I will always to grateful to the amazing staff there. The experiences I have had through Schreyer have allowed me to become a well-rounded person by giving me countless experiences outside of the classroom. I would also like to acknowledge the Erickson Discovery Grant for financial support.

Finally, and most importantly, I want to thank my family. My drive and determination come from my mother, who despite everything always finds a way to be there for her children. My father, who has always taught by example how important it is that the work one does, is not done for oneself, but those around you.

Chapter 1

Motivation: Gas Turbine Combustion Instability

The world took a unified stance against global climate change and its inherent dangers by passing the Paris Agreement in December 2015 [1]. The agreement limits the increase in average global temperature by reducing pollutant gas emissions, such as CO_2 and NO_2. Produced during the power generation process when fossil fuels burn, these gases could be reduced by producing less power. While this solution might solve the climate problem, it would prove detrimental to the world economy as global energy demand constantly increases. However, engineers have already implemented an effective, but challenging, solution. Specifically, natural gas fired gas turbines are operated using a lean premixed combustion process that produces very little NOx and boosts engine efficiency, reducing CO_2. NO_2 is responsible for smog and acid rain and is formed by high combustion temperatures, which is common in older gas turbines [2]. Lean premixed combustion works by premixing the fuel and air mixture upstream of the combustor to create a "lean" mixture, or one that has a larger ratio of air to fuel than would be stoichiometrically recommended. This lean mixture is then ignited inside the combustion chamber. The benefit of using a lean mixture for combustion is that it burns at a lower temperature, which produces less NOx emissions [2]. Unfortunately, lean systems present their own problems. Namely, they are more susceptible to combustion instability.

Combustion instability presents many operational issues for gas turbines, the physics of which will be explored in Chapter 2. The danger of combustion instability events is that they produce large amplitude oscillations in the pressure and velocity field of a combustor. These

oscillations can lead to thrust oscillations, severe system vibration, cyclic stresses, varied thermal loading, flashback, flame blowoff, and a host of other issues that may ultimately be responsible for premature component wear, increased engine emissions, or catastrophic failure [3]. Combustion instability has been responsible for the delay or costly failure of many high intensity combustion devices. The Saturn rocket's initial F-1 engines produced instabilities of up to 100% the mean combustor pressure. This caused unacceptable engine damage and required about 2000 expensive full-scale engine tests to discover a work around for the problem [3]. In 1968, the United States Air Force was forced to undertake the costly removal and repair of many fielded Minuteman Wing I missiles. Five routine missiles tests failed due to complications stemming from combustion instability, putting the entire arsenal in question [3].

Modern day combustion systems, including examples such as Solar Turbines' lean premixed system and Pratt & Whitney's full-annular aeroengine combustors, are still plagued by combustion instability. Solar Turbines' utilizes a lean premixed combustor to reduce flame temperature and therefore reduce NOx emissions. At lean conditions, the flame is close to the lean blowoff limit and operates with reduced stability. It is very sensitive to variations in the fuel-air ratio, which when changed, drastically alter the heat release rate. An oscillating heat release rate increases the probability that the combustion process will trigger acoustic oscillations at the resonance frequency of the system [4]. In the Pratt & Whitney engine, the instability generates an acoustic frequency between 420 Hz, when operating at low power, and 580 Hz, when operating at high power. These oscillations in pressure occur at large enough amplitudes that they cause vibrational stress in the turbine at a level that is unacceptable. It would reduce the life of the engine beyond allowable margins [5].

Chapter 2

Literature Review

Combustion instability is the coupling between flame heat release oscillations and combustor acoustics [3]. Combustors are acoustically receptive and act as resonance chambers. Certain acoustic perturbations may reverberate at a system frequency, couple with other variables within the system, and cause a feedback cycle. Figure 1 shows the stages of the feedback cycle. Flame heat release fluctuations are caused by changes in several flame parameters, including the flame surface area, local equivalence ratio, and flame stretch. These heat release fluctuations can then generate a pressure field, which takes the form of acoustic fluctuations in the combustor [6]. The acoustic oscillations then interact with a coupling mechanism that drives the cycle.

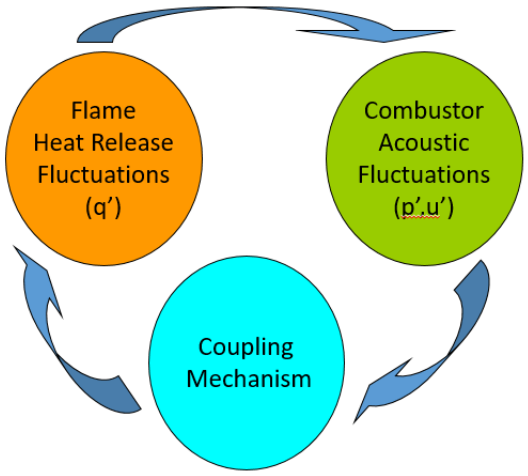

Figure 1: Combustion instability feedback cycle

Due to the complexity of gas turbine combustors, there are various coupling mechanisms that could drive this cycle. This work focuses on swirl-stabilized combustors, which have two main coupling mechanisms: equivalence ratio coupling and velocity coupling. Equivalence ratio

coupling occurs when acoustic oscillations interfere with the fuel and air ratio, leading to unsteady heat release. Velocity coupling occurs when acoustic fluctuations excite velocity perturbations in the flow, which in turn lead to vortex formation and swirl number oscillations that induce a flame response that continues the cycle [6].

Importance of Swirl in Combustion Applications

One challenge that all gas turbines face is keeping a flame stabilized despite changing conditions, both inside and outside of an engine. In order to maintain a flame, the velocity of the incoming gases much be equal to the speed at which the flame propagates. If the incoming gases are moving too quickly, flame blowoff occurs, extinguishing the flame [7]. If the incoming gases are traveling too slowly downstream, the flame travels upstream and out of the combustion chamber, causing an event known as flashback [7]. The inherent challenges within gas turbine combustors are that the incoming gasses always travel faster than the flame speed and the flame must remain stable even as the turbine demands different loads. To combat these issues and maintain a stable flame, designers employ the use of a region of flow reversal that recirculates combustion products in order to promote mixing with and ignition of the reactants [6].

There are many mechanisms used to create this region of flow reversal and high shear, such as bluff bodies, opposing jets, and swirlers. Swirlers, which swirl the fluid as it enters the combustion chamber, are the focus of this work. A typical swirler configuration is shown in Figure 2, which features two concentric radial inflow swirlers, where flow enters the swirler radially and is swirled by aerodynamic turning vanes. Swirling flows have an advantage over the other two mechanisms because swirling flows produce a phenomenon known as vortex

breakdown. Vortex breakdown, which is shown in Figure 3, provides better mixing than the flow patterns produced by either bluff bodies or opposing jets [8].

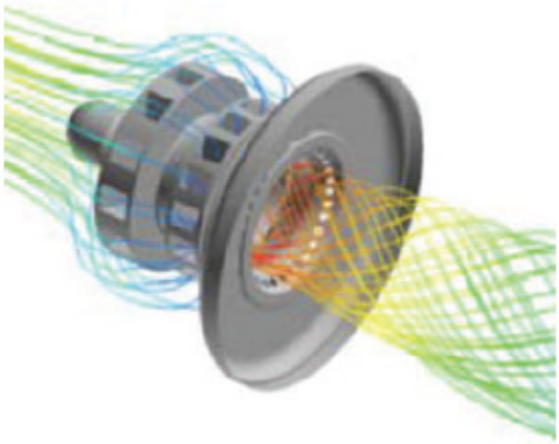

Figure 2: Typical radial entry swirler configuration [9]

Structure of Swirling Flow

Swirling flows are used in combustion applications because of their ability to stabilize and anchor a flame. Flame anchoring occurs in the flow as a result of vortex breakdown [10]. Vortex breakdown is defined when a stagnation point forms on the axis of the flow along with a recirculation region [8]. Figure 3 shows the typical flow paths of a recirculation region. Only half of the flow path is shown since it is assumed to be axisymmetric. *ACBO* contains the recirculation region. Point *B* is the stagnation point, where all flow velocity is zero. The dashed line, *AB*, represents zero axial velocity.

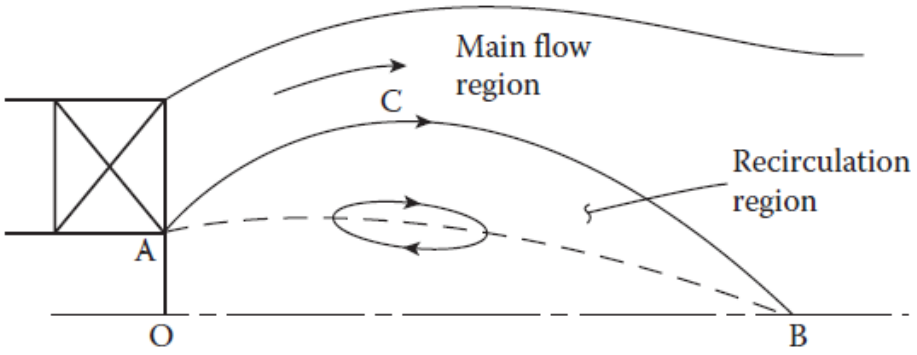

Figure 3: An axial cut of a flow undergoing vortex breakdown [8]

The critical swirl number is the value at which vortex breakdown occurs steadily and is typically just above the upper most value of the intermittent swirl number range. Once vortex breakdown is steady, two shear layers form within the flow (Figure 4). The outer shear layer forms between the external fluid and the spreading jet. The inner shear layer, or wake shear layer, is present between the recirculation zone and the conical jet [8, 11]. As swirl number increases the jet undergoes spreading, which is a radial increase in the size of the jet. The rate of jet spreading is relatively uniform below the critical swirl number. However, once the critical swirl number is surpassed, the rate of jet spreading increases drastically. As well, the axial momentum of the flow downstream decreases as swirl number is increased [11].

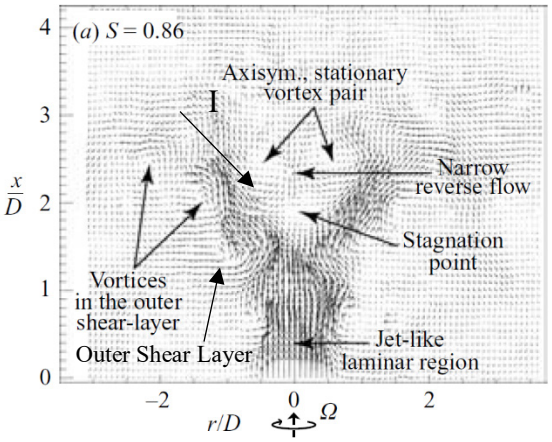

Figure 4: Stable vortex breakdown with formation of shear layers [11]

Three distinct precessing spiral structures exist in unsteady vortex breakdown: primary, inner secondary, and outer secondary vortexes [12]. The primary vortex carries most of the vorticity produced by the swirler and precesses at the smallest radial distance from the nozzle exit. The inner and outer secondary vortices rotate at further radial distances from the nozzle exit, respectively. The interaction of the primary vortex and inner secondary vortex, which are co-rotating co-winding vortices, make up the vortex breakdown zone. It is also important to note that the primary vortex activates the formation of the inner and outer secondary vortices. This dependence makes the shear layers in swirling flows more vulnerable to helical perturbations [12].

Forcing in Swirling Jets

Forcing is one mechanism used to alter the natural progression of vortex breakdown and is similar to the acoustic instability that is present in gas turbine engines. Forcing consists of applying an external force to the flow, often in the form sound waves or using a physical exciter, such as thin shaft [13]. In one study, performed by Lopez, Marques, and Lim [14] forcing has been applied by harmonically modulating a rotating endwall. In their work, they investigate how the spatial oscillations of a vortex breakdown bubble change when the flow is exposed to different forcing amplitudes and frequencies. An important characteristic of a flow undergoing vortex breakdown is its natural frequency, which is the rate at which the vortex breakdown bubble oscillates when under no outside forces. It has been shown that with low amplitude modulation and at a forcing frequency about half that of the natural frequency, the oscillations of the vortex breakdown bubble would increase. Whereas, when modulating the frequency at twice

the natural frequency, vortex breakdown bubble oscillations would be quenched completely [14]. The top row of Figure 5 shows how, at low forcing, the vortex breakdown bubble oscillates in time whereas at high forcing, shown in the bottom row, the vortex breakdown bubble remains spatially uniform.

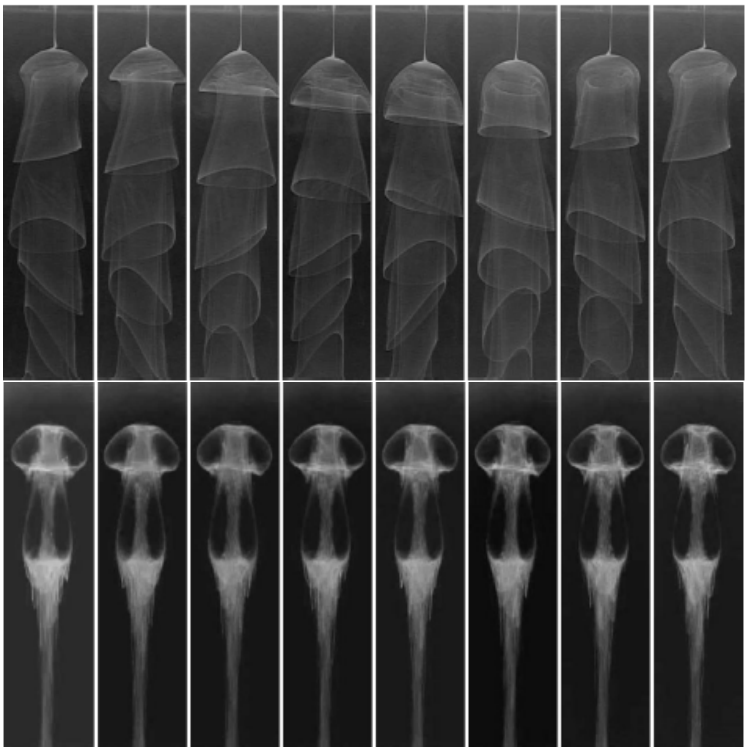

Figure 5: Temporal progression of vortex breakdown oscillations. Low forcing frequency (top), high forcing frequency (bottom) [14]

Precessing Vortex Cores in Swirling Flows

A precessing vortex core (PVC) is a disruptive vortex that naturally oscillates in a swirling flow field. It dominates the flow behavior and moves in a helical pattern about the center of the jet. Figure 6 provides a visualization of PVC in a reacting flow. A PVC forms when the swirl number is above a certain value, higher than the critical swirl number, which indicates

the onset of vortex breakdown [15]. When a PVC is present, it imparts a single, distinct, and narrowband frequency into the flow [16]. This frequency is reflected in both the acoustic emissions from the flow and its velocity field. Syred has shown that the PVC frequency increases linearly with flow velocity [15]. An important tool used to analyze PVCs is proper orthogonal decomposition (POD). POD extracts the highest energy modes from a flow field and produces spatial mode shapes and temporal mode amplitudes [17]. By using POD, the frequency can be extracted from the velocity field by taking the Fourier transform of the temporal modes. Comparing this POD frequency to the frequency recorded by hot-wire-anemometry [16] or pressure transducers [18], one can confirm the existence of a PVC. Visualizing the most energetic spatial modes from POD also allows for PVC identification [16]. Figure 7 shows a characteristic PVC spatial mode as seen by an observer looking normal to the flow. The dotted circle outlines the nozzle location.

Figure 6: PVC visualization in a reacting flow [15]

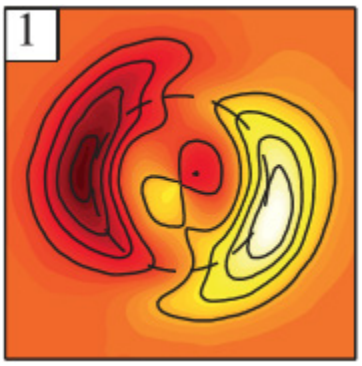

Figure 7: Characteristic spatial mode identifying a PVC [16]

Oberleithner *et al.* modeled the three-dimensional shape of a PVC by using various computational techniques [16]. Figure 8 presents one of these visualizations. A PVC is located between the edge of the recirculation zone and the inner shear layer of a swirling flow undergoing vortex breakdown [11, 16]. The blue helix in Figure 8 represents the PVC. The PVC is a co-rotating and counter-winding structure [11, 16]. The yellow streamlines and grey linear integral convulsion surfaces were determined from time averaged experimental data and show the rotation of the base-flow as well as the location of the recirculation bubble [16]. Though impossible to show in a still image, the presence of a PVC causes precession of the recirculation bubble, in phase with the PVC, about the jet center.

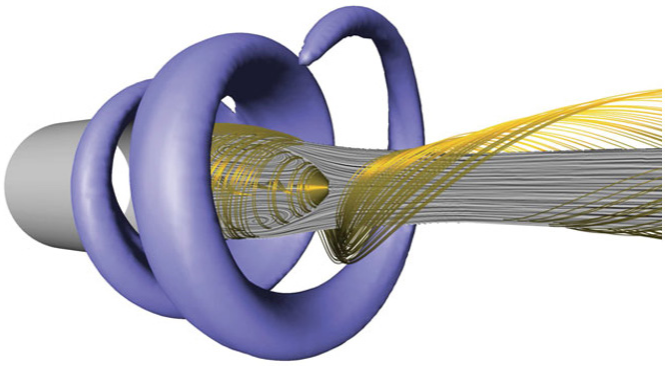

Figure 8: 3-D Flow Field Visualization of the PVC or global mode *m=1* [16]

Despite the PVC being inherently a non-uniform and not fully understood structure, it has practical uses in swirling flows. Firstly, it is important for flame stabilization in reacting flows. The violent oscillatory nature of a PVC, coupled with its location inside the flow, leads to better flame anchoring [9]. Enhanced mixing occurs because the PVC exists between the hot combustion products within the center recirculation zone and the cold reactants in the surrounding jet. The PVC forces the products and reactants to merge, which promotes a more stable flame.

The presence of a PVC can impact a number of different motions of the flow field. By examining azimuthal cuts of unforced, highly swirling flows, O'Connor and Lieuwen [19] identified two self-excited motions as (1) an overall fluctuation of the jet shape and (2) the precession of two coherent smaller-scale structures contained in the central recirculation zone. Figure 9 shows an interpretation of these two motions. The first motion shows the eccentricity of the jet shape pulsing as the jet rotates. With each single rotation about the jet center the jet shape pulses twice before changing pulse direction. For example, at t=4.1 ms and t=13.1 ms the jet shape has turned into a more elliptical feature than neighboring instances in time. The period of rotation of a single jet shape disturbance is about 10 ms, which corresponds to an azimuthal mode number of m=*-2*.

The second motion, the precession of the two coherent structures about the jet center within the recirculation zone is also interpreted in Figure 9. During the first half of this period the structures overlap, while as during the second half they move apart. The period of this motion is twice that of the first motion, about 20 ms total [19]. The azimuthal mode number identifying this motion is m=*-1*. Similar motions were seen in a high-fidelity simulation of swirling flow by

Yang [20]. Figure 10 provides more insight as to the behavior of mode *m=-1*. Mode *m=-1* and *+1* represent spinning modes with a period of one oscillation per rotation about the flow. These modes are non-axisymmetric. Mode *m=0* refers to axisymmetric motion of the flow field, when the entire field is oscillating uniformly.

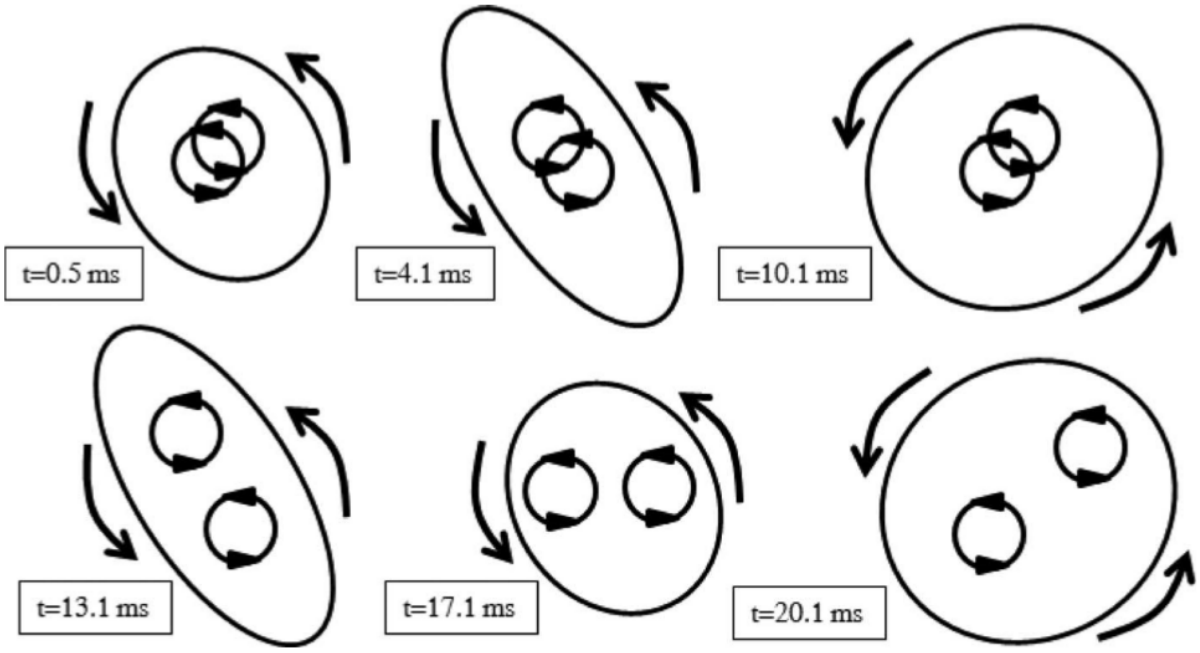

Figure 9: Self-excited motions of jet deformation (*m=-2)* and coherent structures *(m=-1)* due to the presence of a PVC [19]

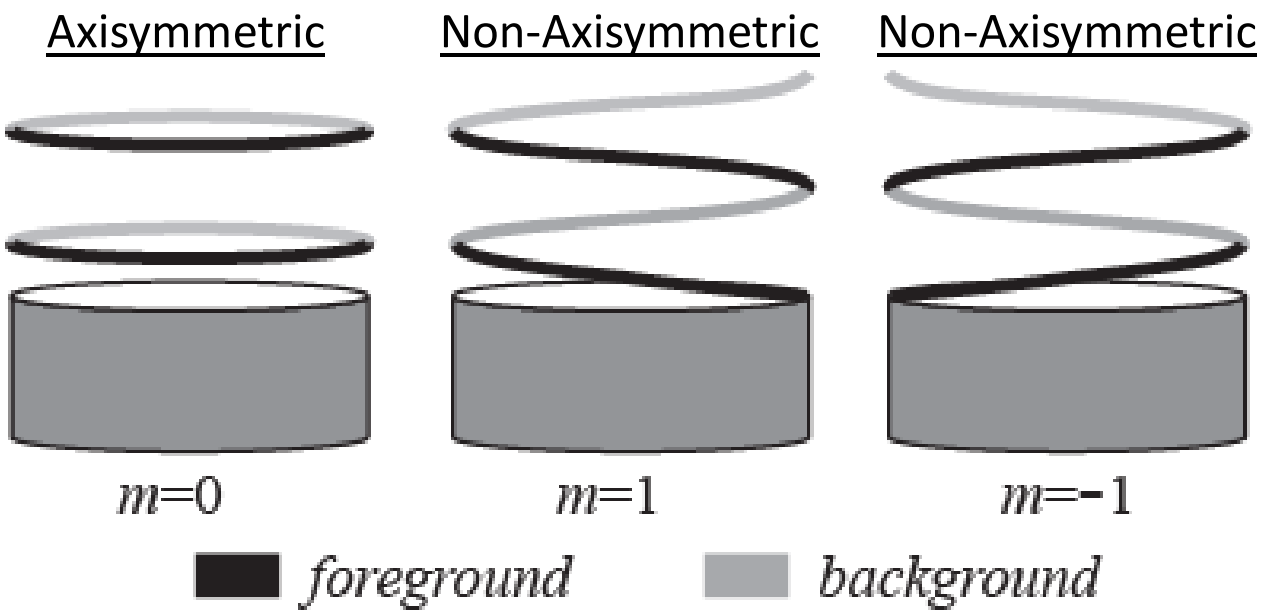

Figure 10: Mode numbers of characteristic disturbance field in swirling flows

Azimuthal spatial mode decomposition can be used to determine the spatial mode shape as a function of radial distance from the center of the jet. Figure 11 shows the output of this analysis technique, which was performed by O'Connor and Lieuwen on the same data being represented in Figure 10. Figure 11 shows the clear presence of modes *m=-2* and *m -1*. If the decomposition were performed closer to the nozzle, the mode *m=-1* would dominate as the center region of the jet is preeminently composed of motion from the precessing coherent structures. Moving radially outward past *r/D=0.7* leads to the strength of all modes swiftly decaying. The lack of an *m=0* response indicates the high level of non-axisymmetric behavior that a PVC imparts on a flow.

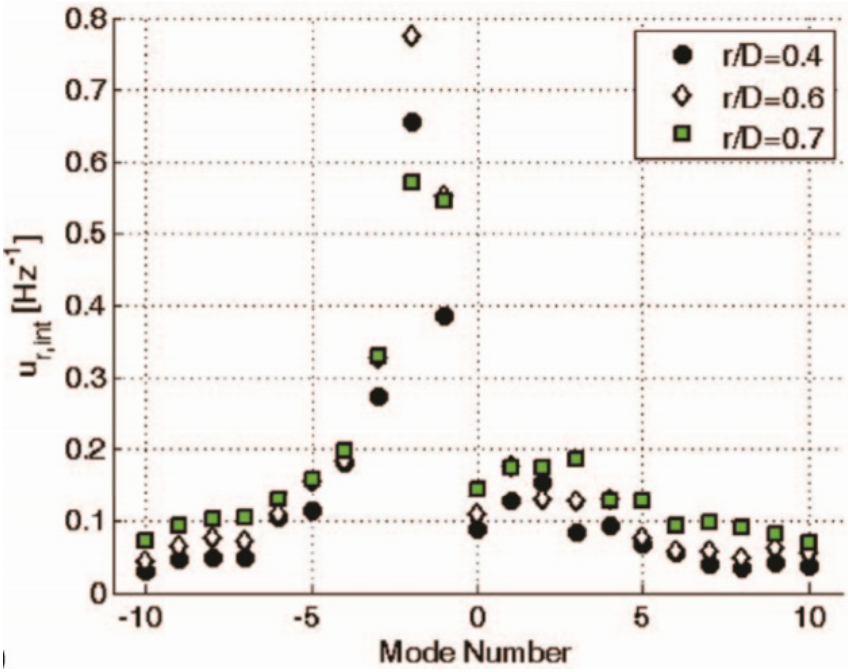

Figure 11: Spatial mode energy distribution at three radii of a flow field containing a PVC [19]

Research Goal

The goal of this work is the study the natural dynamics of a PVC for the purpose of using it to eliminate the issue of combustion instability in swirling flows. Basic parameters of the PVC, such as its oscillating frequency and amplitude dependence will be explored. Previous work has suggested that the presence of a PVC creates a flow field which is impervious to acoustic forcing [18]. This new study will rigorously explore different forcing conditions to determine the impact a PVC has on the flow's response. If a swirling flow no longer responds to acoustic forcing, then the combustion instability cycle would be severed. A combination of experimental and theoretical tools will be used first to determine if flow field receptivity suppression is occurring and then to explain the mechanisms that allows this suppression to occur.

Chapter 3

Experimental Facility

Design Overview

Swirling flows with strong enough swirl experience vortex breakdown, produce an area of flow recirculation, and create conditions that allow a flame to remain stably lit. The usefulness of these flows has created a scenario where swirling flows are implemented used in every gas turbine. This makes it imperative that they are understood on a fundamental level. The experiment used in this work controls three governing parameters of swirling flows that allow for fundamental information to be gathered.

The degree of swirl imparted into the flow has a drastic effect on the structure of the swirling flow field. For this reason, a variable angle radial entry swirler is used to independently control swirl number, while holding all other system variables constant. Flow velocity is controlled by use of a needle value. Changes in flow velocity will alter the Reynolds number of the flow. To introduce an acoustic field and mimic the effects of combustion instability on the flow field, speakers are placed at the base of the experiment to provide acoustic forcing. To non-intrusively quantify the acoustics at a location near the swirling flow, the nozzle of the experiment features two ports for pressure transducers to be placed. The experiment produces an open jet, which is capable of being studied by multiple forms of laser diagnostics. Unimpeded access to the flow field allows for the velocity field to be captured from various angles using high speed imaging techniques. More details of the key design parameters and experimental diagnostics will be presented after an overview of the physical experiment.

Experimental Rig Design

The experiment was designed to keep the mechanics and flow path simple as to allow for the fluid mechanics of interest to be easily studied. Figure 12 shows a solid model of the experiment with key features called out. Room temperature air enters the experiment via the 4" air inlet port at the bottom of the rig. Upstream of this inlet, the air has passed by a flow meter and several valves used to set the desired mass flow rate. The air then travels by two Gall siren forcing speakers used to provide longitudinal acoustic forcing. The speakers can be controlled in both frequency and amplitude. After passing the speakers, the air enters a settling chamber that is 6" in diameter and has perforated plates at both ends to even out any turbulent structures that may be present in the flow. A 6" to 3" smooth contraction is used to shape flow and create a radially uniform velocity distribution before the flow enters the swirler's chamber. The flow enters the variable angle radial entry swirler, shown in the bottom right image of Figure 12,

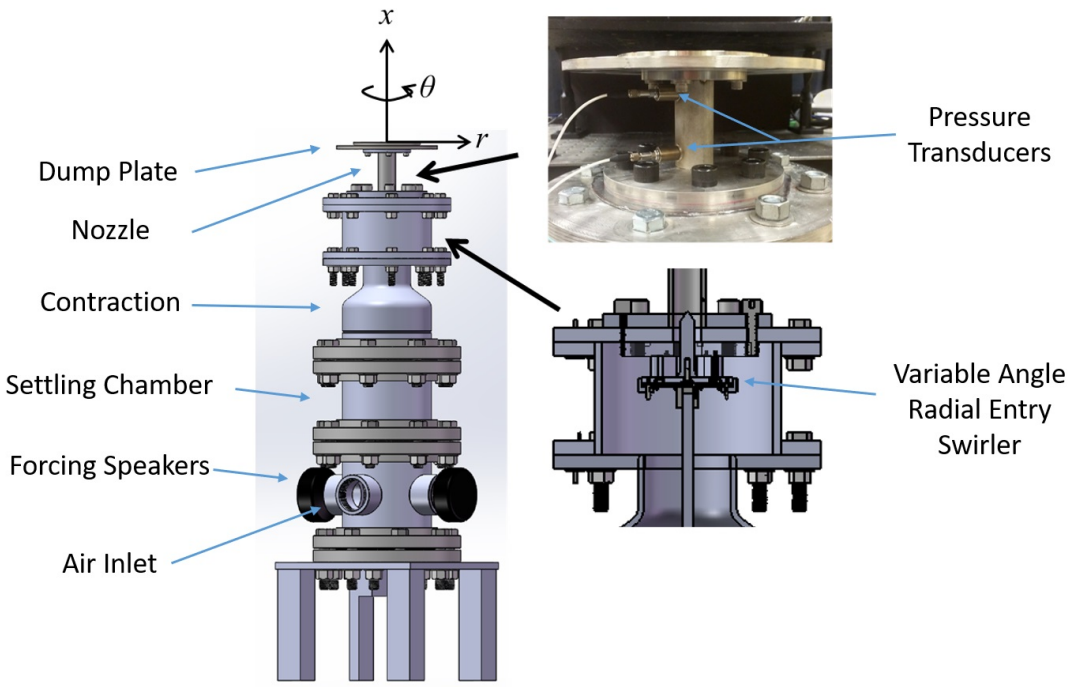

Figure 12: Swirling test rig

radially and exits axially. Swirl is imparted on the flow by deflecting the air azimuthally at a specified geometric angle, defined by the swirler blades. The now swirling air travels through the 1" diameter nozzle of the experiment. Within this nozzle are taps for two pressure transducers, as show in the top right image of Figure 12. The flow then exits into the atmosphere at the dump plane.

The variable angle radial entry swirler, shown in detail in Figure 13, is the heart of this experiment. It allows for the swirl number of the flow to be changed independently, without changing the mass flow rate, Reynolds number, or turbulence intensity. The swirler consists of eight evenly spaced NACA 0025 airfoils that are 1" tall and 1" in chord length [21]. The blades are rotated by using a two-plate system. The Top Plate, labeled in Figure 13, has curved guide slits which the airfoils rest in. The Top Plate is held stationary while the Bottom Plate, which has straight slits, is rotated. The Bottom Plate is rotated by means of a shaft that runs the down the entire length of the experiment and is actuated by stepper motor mounted to the base.

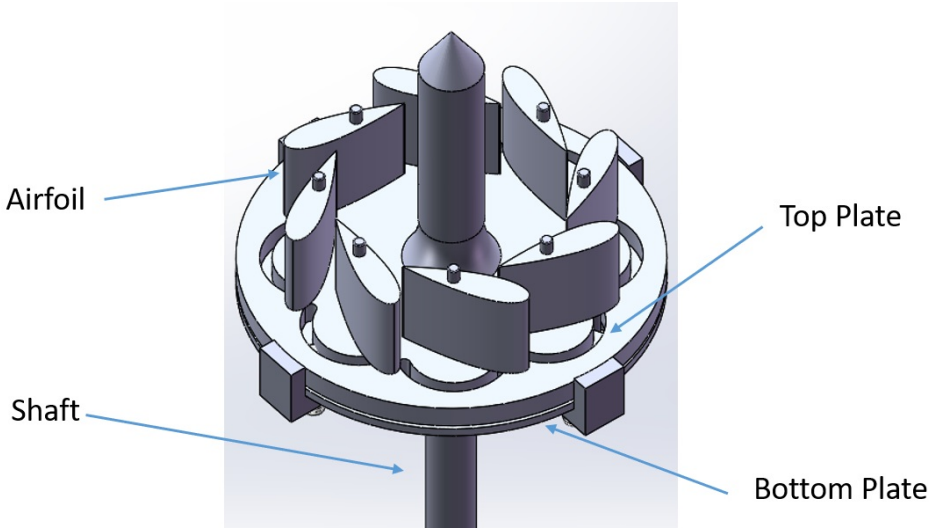

Figure 13: Swirler

The range of angles that can be covered by this swirler is -70° to 70°. The swirl angle is set visually by looking through plug holes drilled about the circumference of the swirl chamber. Each airfoil has a vertical line etched down its leading edge. The Top Plate has vertical guide lines etched at 5° increments from -70° to 70°. By lining up the airfoil leading edge with the Top Plate guide lines the geometric swirl number can be set with a 2.5° resolution. Figure 14 shows a picture of one of the airfoils inside the swirler with the airfoil leading edge and Top Plate guide lines called out. Repeatability tests were run to verify that airfoils were capable of being set at the same angle consistently.

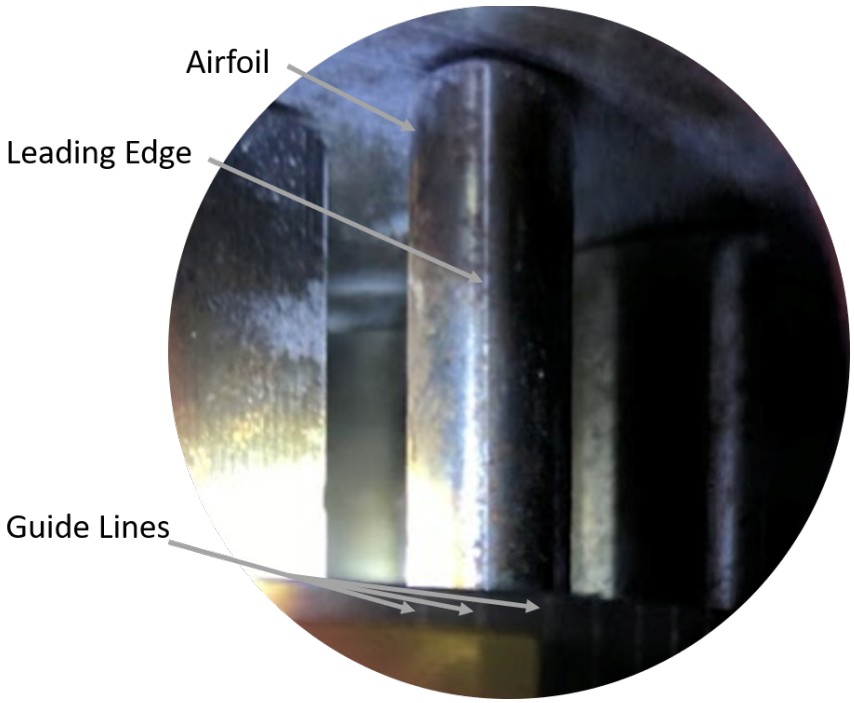

Figure 14: Airfoil inside swirler

Acoustic Forcing

Acoustic forcing in this experiment is provided by two sirens located at the base of the rig, as shown in Figure 12. The sirens are Galls SK144 100 W speakers. These sirens are traditionally used on emergency vehicles, such as police cars. However, they have proven useful in experimental situations because of their ability to maintain a set frequency across a wide range of amplitudes and produce a wide range of frequencies. Additionally, the frequency and amplitude ranges produced are relevant to conditions experienced in fielded gas turbine combustors. The frequency range of these sirens is 100-15000 Hz and the power output can be set between 0.1 W and 50 W. The frequency is set through a LabView program that controls the sirens. The power is set using a combination of the LabView program and external power amplifiers. In this work, the speakers are always operated in phase, at the same frequency, and at the same power to produce longitudinal acoustic forcing. Longitudinal forcing produces an axisymmetric pressure wave, as shown in mode $m=0$ of Figure 10.

Diagnostics

Frequency Analysis

Swirling flows produce and are sensitive to acoustic fields. To study these fields, frequency analysis is performed on the pressure signal captured by two pressure transducers located in the nozzle of the experiment, as shown in Figure 12. The pressure transducers (PT) are located 2.54 cm and 7.62 cm downstream of the swirler, and 6.92 cm and 1.84 cm from the nozzle exit, respectively. In the remainder of this paper, the location of the pressure transducer

located closer to the nozzle exit will be referred to as “near nozzle,” and the location of other pressure transducer as “near swirler.” PCB Piezotronics model 113B28 pressure transducers are used. The pressure transducer signal is amplified using PCB Piezotronics four channel, ICP sensor signal conditioner, model 482C26. The pressure signal is recorded using LabView through an National Instruments DAQ at 20kHz for a duration of 3 seconds. However, LabView records the voltage output from the pressure transducers as a function of time. In order to perform frequency analysis, the data is converted to single sided power spectral density.

The first step in this frequency analysis is to decide on the number of ensembles to average over. In this experiment, a pressure transducer records 60,000 data points and the data is averaged of 30 ensembles, leaving a frequency resolution on 10 Hz. Beginning with the time series of the voltage output, $x(t)$, the following process is used. The voltages are first converted to units of pounds per square inch, PSI:

$$x_n = \frac{x(t)}{(PT_{sens})(Gain)}$$

where x_n is indexed for each sampled time, PT_{sens} is the sensitivity of the pressure transducer, and $Gain$ is the amplification factor set on the signal conditioner.

The data must next be split up into 30 ensembles, each with the same number of elements. In this experiment there are 2,000 elements in each ensemble.

$$x_{e,i} = [x_1 : x_{2000}, x_{2001} : x_{4000,} \dots, x_{58001} : x_{60000}]$$

x_e is the collection of all ensembles of x and i is the index of each ensemble. The mean value is then subtracted to obtain the fluctuating pressure over time.

$$x_{fluc,i} = x_{e,i} - \bar{x}$$

x_{fluc} is the fluctuating pressure divided into ensembles.

To transform the temporally resolved data into the frequency domain, the Discrete Fourier Transform (DFT) is performed on each ensemble of x_{fluc}:

$$X_{e,i,m} = \sum_{i=1}^{I} \sum_{n=1}^{N} x_{fluc,i,n} e^{-j2\pi \frac{nm}{N}} \Delta t$$

where I is the total number of ensembles, N is the total number of elements in each ensemble, n is the index for the sampled time series, m is the index for the sampled spectrum (serves the same purpose as n except in frequency space), Δt is the time between each time sample, or the inverse of the sampling frequency, and X_e is the pressure data in frequency space divided into ensembles. For the purposes of calculation, the above equation can be solved in MATLAB using the command $fft * \Delta t$. At this point the ensembles are averaged together to amplify coherent frequencies:

$$X_m = \overline{X_{e,i,m}}$$

Taking the DFT produces a series of complex numbers which must be accounted for when computing the single sided spectral density, G_{xx}:

$$G_{xx} \equiv \frac{2}{T} |X_m|^2 \quad for \quad 2 \leq m \leq \frac{N}{2}$$

$$G_{xx}|_{m=1} \equiv \frac{1}{T} |X_0|^2 \quad and \quad G_{xx}|_{m=\frac{N}{2}+1} \equiv \frac{1}{T} \left| X_{\frac{N}{2}+1} \right|^2$$

where T is total time it takes to sample one ensemble of data points. Finally, the proper units are obtained, which represent solely the amplitude of the signal:

$$P_{rms} = \sqrt{\frac{G_{xx}}{T}}$$

where P_{rms} is the ensemble averaged pressure signal.

Particle Image Velocimetry

Particle Image Velocimetry (PIV) is a high-speed laser diagnostic technique used to image the flow field and measure two or three components of velocity. The technique uses a high-power laser sheet to illuminate seeding particles that have been mixed into the flow field. The illuminated plane is then imaged with a high-speed camera(s). In the experimental setup studied in this work, there are two common planes that are illuminated, as shown in Figure 15. The *r-θ* plane is shown in Figure 15a and is illuminated by creating a horizontal laser sheet. The *r-x* plane is shown in Figure 15b and is illuminated by creating a vertical laser sheet. A cylindrical coordinate system is used, as illustrated in Figure 12 . The azimuthal and radial velocity is mapped when capturing data in the *r-θ* plane. Whereas in the *r-x* plane, the radial and streamwise velocity is mapped, as well as the velocity normal to the laser plane.

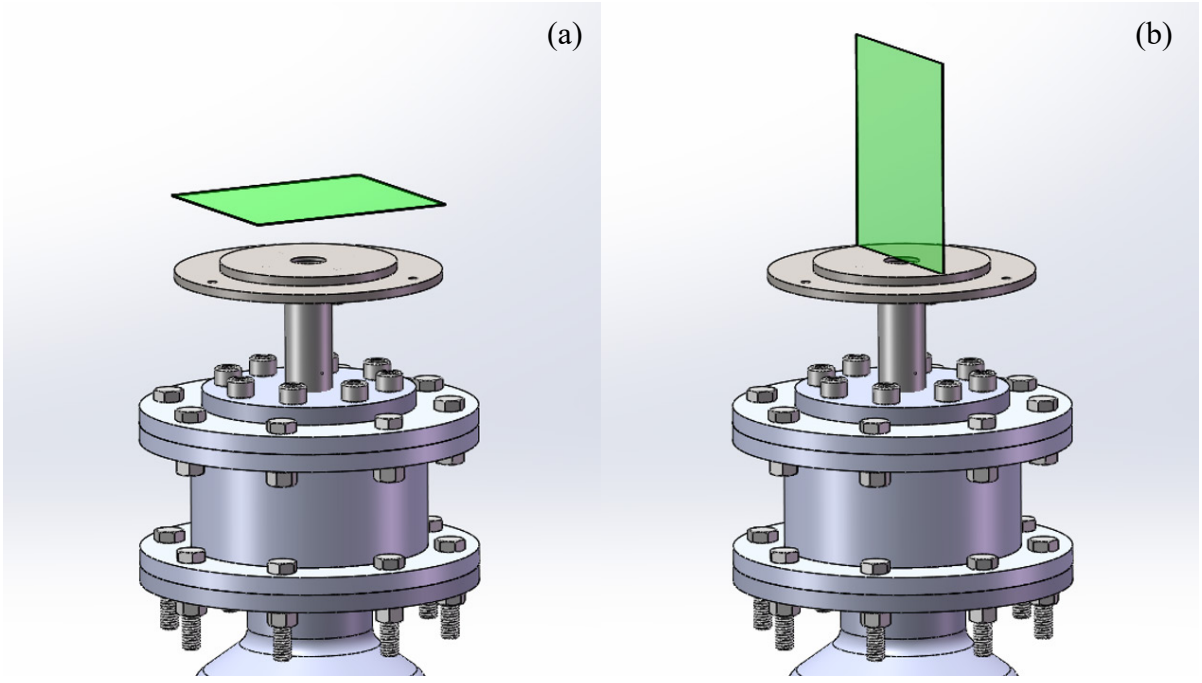

Figure 15: Laser sheet, shown in green, oriented in the *r-θ* plane (a) and the *r-x* plane (b)

In this study, velocity fields are captured in the *r*-θ plane using PIV with images from an SA5 Photron complementary metal oxide semiconductor (CMOS) high speed camera, set in double-frame mode. In order to capture images in the *r*-θ plane the camera must be looking directly normal to the illuminated sheet. Due to the challenges of mounting a camera directly above the flow field, a parabolic mirror set up was designed to allow for safer camera placement. Figure 16 shows the set up surrounding the experiment. The camera is mounted on a table with the lens in the *r*–*x* plane, and the laser plane is imaged using a periscope configuration. The lens points directly at an aluminum coated, right angle, first surface mirror, mounted 25.4 cm away. The mirror is suspended 46.3 cm directly above the nozzle. The dimensions of the mirror face are 75 mm by 106.1 mm. The mirror redirects the field of view of the camera such that it is shifted 90° from the *r*–*x* plane and captures the *r*-θ plane.

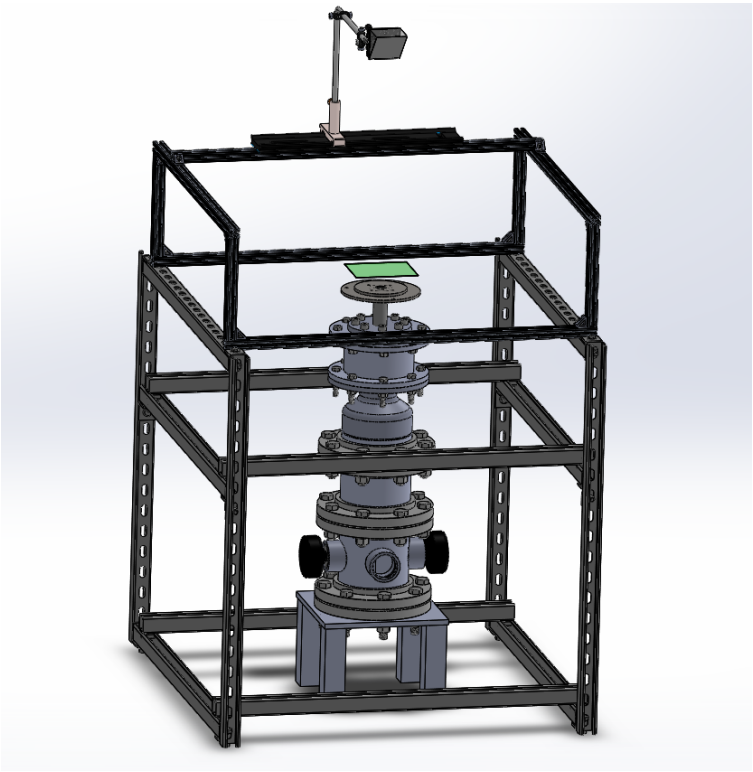

Figure 16: Parabolic mirror set up to take data in the *r*-θ plane

A Hawk/Darwin Duo Nd-YAG, 532 nm wavelength, 60 W laser is used for PIV. For all cases tested, the laser is directed through a 50 mm sheet optics to produce a laser sheet in the *r-θ* plane. The laser sheet is set to a height of *x/D=1.7*, which is twice the convective wavelength of the vorticity fluctuations produced with 600 Hz forcing. This convective wavelength was determined in work performed by Mathews *et al*. [18] and choosing this laser plane allows for direct comparisons of the *r-θ* data in this study and the velocity describing functions at 600 Hz reported in Mathews *et al*.

The sampling rate of the PIV system is 5 kHz, with an interframe time ranging from 17 to 23 μs depending on swirl number. Images are recorded for a 1 sec duration, yielding 5000 frames per test case. The PIV system is triggered simultaneously with the PTs. Aluminum oxide particles with a nominal diameter of 1–2 μm are used as tracer particles and can accurately follow flow perturbations up to a frequency of 4000 Hz. Velocity vectors are calculated in DaVis 8.3.1 without any preprocessing or masking. Cross-correlation with multi-pass iterations with decreasing window sizes is used. The first pass is a 32x32 pixel interrogation window with a 50% overlap followed by two passes with a 16x16 pixel interrogation with a 50% overlap. During vector post processing, there are two methods used to reject vectors. First, if the vector is more than three times the RMS of the surrounding vectors, the vector is removed and replaced. Additionally, universal outlier detection removes and replaces spurious vector results.

Data Analysis

Proper Orthogonal Decomposition

Proper Orthogonal Decomposition (POD) is a modal decomposition technique used to extract the most energetic motions in the flow field [17]. POD is performed on the fluctuating velocity field generated from PIV; the time-averaged field is subtracted initially. POD breaks the flow into corresponding spatial, temporal, and energetic components. An eigenvalue decomposition is used to calculate the POD. The spatial modes produce mode shapes that represent coherent flow structures. The power spectral density of the temporal modes is found to analyze each mode in the frequency space. The energetic component is used to compare relative mode strengths and determine which modes dominate flow field motion. In the case of this study, POD is performed on the radial and azimuthal component velocities at each instant in time.

Azimuthal Decomposition

Azimuthal mode decomposition is used to interpret the motion of the disturbances in the r-θ plane. This decomposition requires that the velocity field be mapped on a cylindrical coordinate system. Figure 17 shows an example time averaged velocity magnitude field with the points that make up the cylindrical grid in the r-θ plane.

The cylindrical vector field is calculated by performing a cubic spline interpolation on the Cartesian vector field at each of the white dots in Figure 17. A third-order fit was found to most accurately represent the data by comparing interpolated points to known values. In the case

of this study, the cylindrical grid is formed with 32 radial increments and 120 azimuthal increments. The number of increments was calculated to maintain the spatial resolution that was captured with the Cartesian grid from the PIV system at the nozzle radius. At radii smaller than that of the nozzle, the resolution is increased, and at radii larger than that of the nozzle, the resolution is decreased.

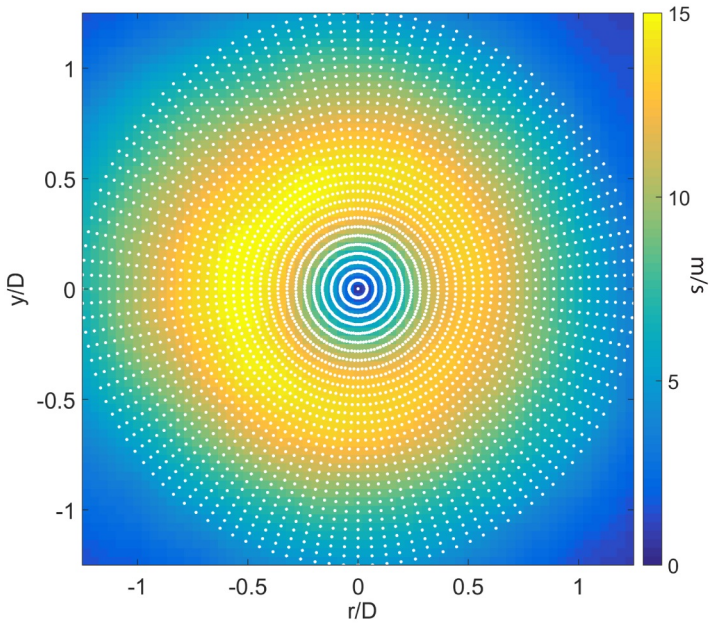

Figure 17: Interpolated points in cylindrical coordinates (white dots) on velocity magnitude in the *r-θ* plane

The velocity field at each radius of the data is decomposed in cylindrical coordinates using the equation below, where $\hat{B}_{i,m}$ is the strength of the azimuthal mode, m, which is derived from the fluctuation velocity field, u', at each frequency, ω

$$\hat{B}_{i,m}(r,x,\omega) = \frac{1}{2\pi}\int_0^{2\pi} \hat{u}_i'(r,x,\theta,\omega)e^{-im\theta}d\theta$$

The resulting modes represent motions of varying levels of axisymmetry in the flow field. For example, mode *m=0* describes axisymmetric motion in the flow field; the acoustic forcing

used in this study should result in *m=0* motion as the forcing is longitudinal. Modes *m=1* and *m=-1* are representative of spinning modes in opposite directions with a "period" of one oscillation around the circumference of the flow [22]. Figure 10 shows a depiction of these mode behaviors.

Theoretical Formulation

In order to determine how the physical presence of the PVC affects the flow field's response to forcing, a linearized hydrodynamic stability analysis is performed. This work was not performed solely by the author and was done in collaboration with Dr. Hemchandra at Indian Institute of Science in Bangalore, India, who analyzed the flow fields obtained from the experiment used in this study. To determine the coherent oscillating field around the time-averaged base flow, a linearized Navier-Stokes equation is used, which is derived below. Firstly, the coherent fluctuations of the instantaneous quantities, which are the radial velocity, streamwise velocity, azimuthal velocity, and hydrodynamic pressure, are isolated by subtracting off the time average and then neglecting nonlinear terms of each quantity. These quantities are then applied in the Navier-Stokes equation:

$$\frac{\partial \vec{u}}{\partial t} + \vec{u} \cdot \nabla \vec{u} = -\frac{\nabla p}{\rho} + \upsilon \nabla^2 \vec{u}$$

The fluctuating pressure and velocity terms are solved for and are represented as follows:

$$u' = Ae^{-ik^+ t} e^{-i\omega t}$$

$$p' = Ae^{-ik^+ t} e^{-i\omega t}$$

where A is the signal amplitude, $k^+$is spatial wave number of the downstream-propagating disturbances, and ω is the excitation frequency.

To study the spatial growth or decay of disturbances in the shear layer, the k^+ term is decomposed into its real and imaginary components:

$$k^+ = {k_r}^+ + i{k_i}^+$$

If ${k_i}^+ < 0$ then the coherent fluctuations within the shear layer are identified as growing spatially. A similar method is used to quantify the temporal growth of the instability, or PVC. The ω term is broken out into its real and imaginary components:

$$\omega = \omega_r + i\omega_i$$

If $\omega_i > 0$ then the PVC is growing in time.

Chapter 4

Acoustic Characterization

Swirling flows both produce and are susceptible to, in some cases, external acoustic excitation. As shown in Figure 1, acoustic fluctuations are a key component of understating the combustion instability feedback cycle. In no real combustion environment, just as in this study, do the acoustics of the flow field exist in isolation. They interact with the combustion chamber itself, or in the case of this study, the experimental rig. It is important to understand the acoustic contribution of the rig to the acoustic excitation at the nozzle exit, where it first interacts with the flow field, in order to determine what is generating the signal that is recorded in the pressure spectrum.

To determine the experimental rig contribution to the acoustic field, an acoustic characterization is performed. An acoustic characterization involves perturbing the experimental rig in the absence of any flow. Having flow would cause a flow-induced pressure signal. To perform this characterization, the two forcing speakers located at the base of the rig (see Figure 12) are used to generate a range of frequencies. Specifically, a frequency sweep is performed between 560 – 1800 Hz in increments of 20 Hz. The speakers are used at the same forcing power of 10 W and are operated in phase. The pressure signal is recorded using the two pressure transducers located in the nozzle of the experiment. The temporal pressure signal is converted into a pressure spectrum using the process described in the Frequency Analysis section. Figure 18 shows the results of the acoustic characterization with the swirler set to 65°.

The forcing sweep, in Figure 18, shows the frequencies that are amplified by the rig. When being forced between 560–680 Hz and 800–940 Hz the rig is not receptive and does not

amplify these frequencies. From 680-780 Hz there is a small response. Between 1000-1100 Hz there is a large response that will appear in pressure signals presented later in this work. Above 1200 Hz the response of the rig begins to increase. At about 1360 Hz the acoustic amplitude seen by each pressure transducer begins to diverge. This divergence is due to the fact that as frequency increases, acoustic wavelength decreases; at the frequencies above 1360 Hz, the distance between the two pressure transducers is no longer small as compared to the acoustic wavelength, as it is at lower frequencies, and so the two pressure transducers measure two different parts of the standing acoustic wave in the rig, resulting in different pressure fluctuation amplitudes. The trend between the two lines is identical, however, showing the overall response of the system well even at these high frequencies. However, the frequencies of interest in this study lie primarily between 600 Hz and 1200 Hz, and so results between the two pressure sensors in the nozzle can be seen as relatively identical.

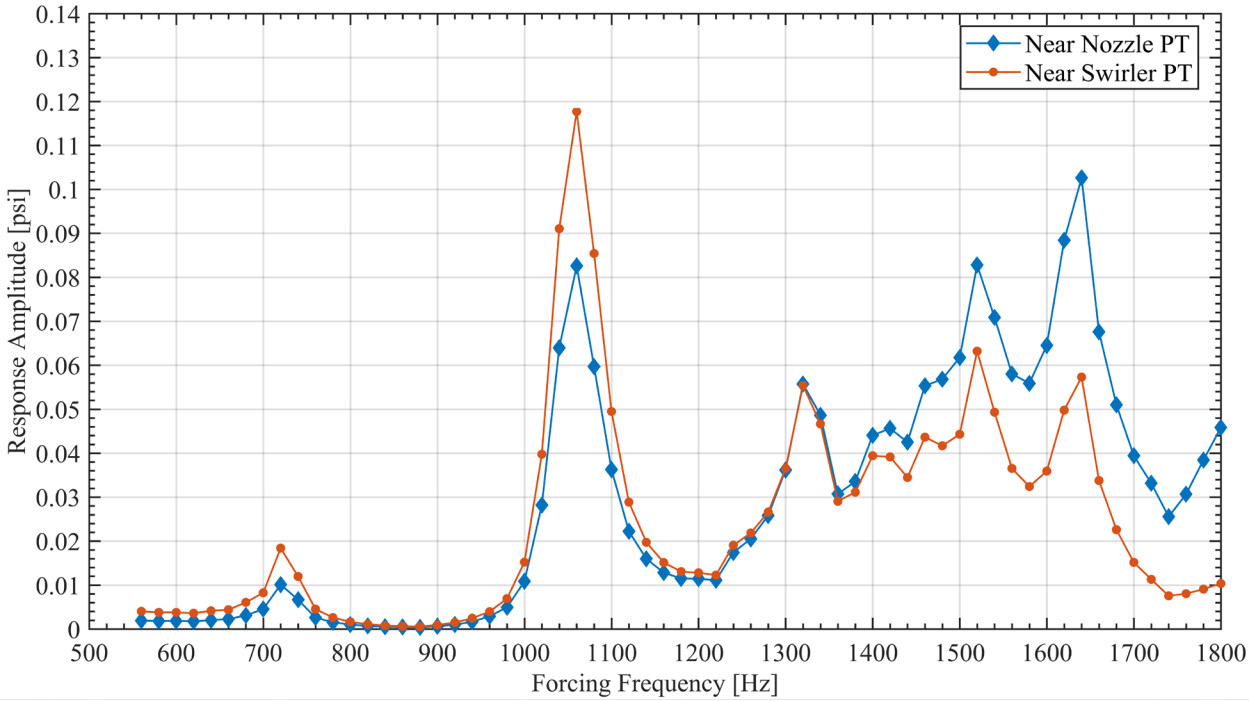

Figure 18: Acoustic characterization of rig at 65°

The results shown in Figure 18 allow for the acoustic field generated when air is flowing to be understood within the context of the acoustics generated by the rig itself. For example, any pressure signal that the flow produces between 1000-1100 Hz will clearly be amplified by the rig. Whereas, if a large 850 Hz signal appears in the pressure spectrum, it is known that the frequency is a consequence of the flow field itself and not the rig.

The results shown in Figure 18 were gathered only for one blade angle, 65°. However, the rig is operated at multiple blade angles and it is possible that a different blade angle will lead to a different pressure response. This is because changing the blade angle of the swirler alters the geometry of the experiment. Different geometries can lead to different acoustic impedances. To study the effect of changing the blade angle, another acoustic characterization was performed with the swirler set to 55°. The results are presented in Figure 19 in conjunction with the characterization results from 65°. It is clear that there is no significant difference in acoustic response when the swirler is set at different blade angles. The results from these two characterizations will be extrapolated to all other high swirl number cases in this work, where the acoustic field is important.

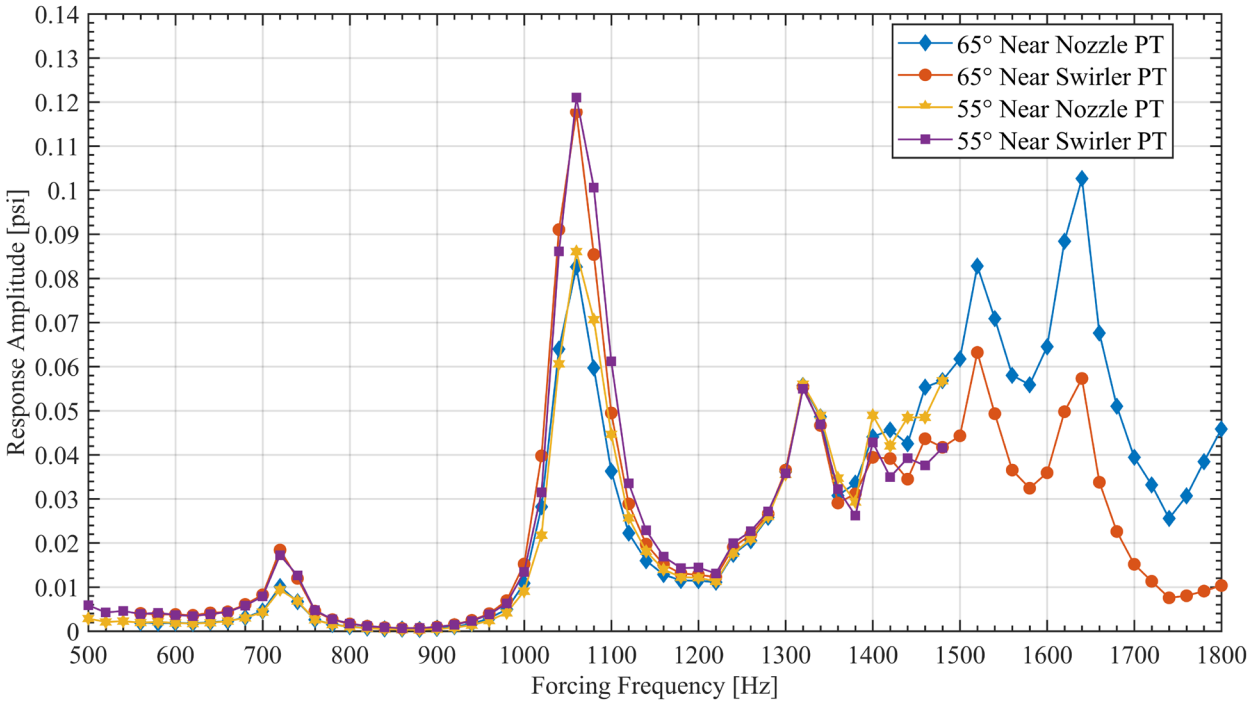

Figure 19: Acoustic characterization of rig at 55°

Chapter 5

Precessing Vortex Core Characterization

Swirl Number Clarification

Before presenting results pertaining to the swirling flow field, an understanding of the swirl number, as it is used in this work, is required. The swirl number is a ratio of axial flux of swirling momentum to the axial flux of axial momentum. The general definition of the swirl number is

$$S = \frac{\int_0^R u_x u_\theta r^2 dr}{R \int_0^R u_x^2 r dr},$$

where S is the swirl number, R is the radius, u_x is the axial velocity, and u_θ is the azimuthal velocity. However, this definition requires intensive flow field measurements. For axial swirlers, such as the one used in this experiment, it is conventional to assume the streamwise velocity at the nozzle exit has a perfectly flat profile and that blade angle of the airfoils defines the tangential velocity of the flow [9]. These assumptions, once applied to the general definition, lead to the following simplified equation, known as the geometric swirl number:

$$S = \frac{2}{3}\tan(\beta),$$

where β is the blade angle of the axial swirler blades. The geometric swirl number is used in the remainder of this work. Chapter 3 discusses that the blade angle range of the swirler is ±70°. When converted to geometric swirl number, the range of possible swirl numbers becomes -1.83 to 1.83. An angle of 0° and a geometric swirl number of 0 correspond to a pure jet, with no component of azimuthal or radial velocity.

Frequency Characteristics of the PVC

When a PVC is present in a swirling flow, it produces an audible and distinct frequency. The pressure transducers placed in the nozzle of this experiment are used to study how this frequency changes as the flow conditions change. There are two factors that alter this frequency: the flow rate and the swirl number. Figure 20 presents the frequency spectra for various cases where both the swirl number and flow rate are changed.

Three swirl numbers are presented in Figure 20, all of which produce a PVC. The PVC is the distinct triangular peak on all plots and is called out by a blue arrow. The plots also show a frequency bump around 1000 Hz, which is attributed to the acoustics of the rig, shown in Figure 18. The PVC frequency is measured by the near-nozzle pressure transducer and only produces a small response in the near swirler pressure transducer. As the swirl number is increased at a fixed flow rate, both the amplitude and frequency of the PVC increase without changing the characteristics of the rest of the spectrum. When the flow rate is increased at a fixed swirl number, the PVC frequency increases as well as the amplitude of the entire spectrum. This increase in overall spectrum power is due to the additional noise generated by the higher turbulence intensity present in higher velocity jets. The PVC frequency is independent of the rig acoustics discussed in Chapter 4. The rig acoustics do not entrain or otherwise change the frequency response of the PVC, which appears to exist on top of and move through the strong rig response from 1000-1100 Hz.

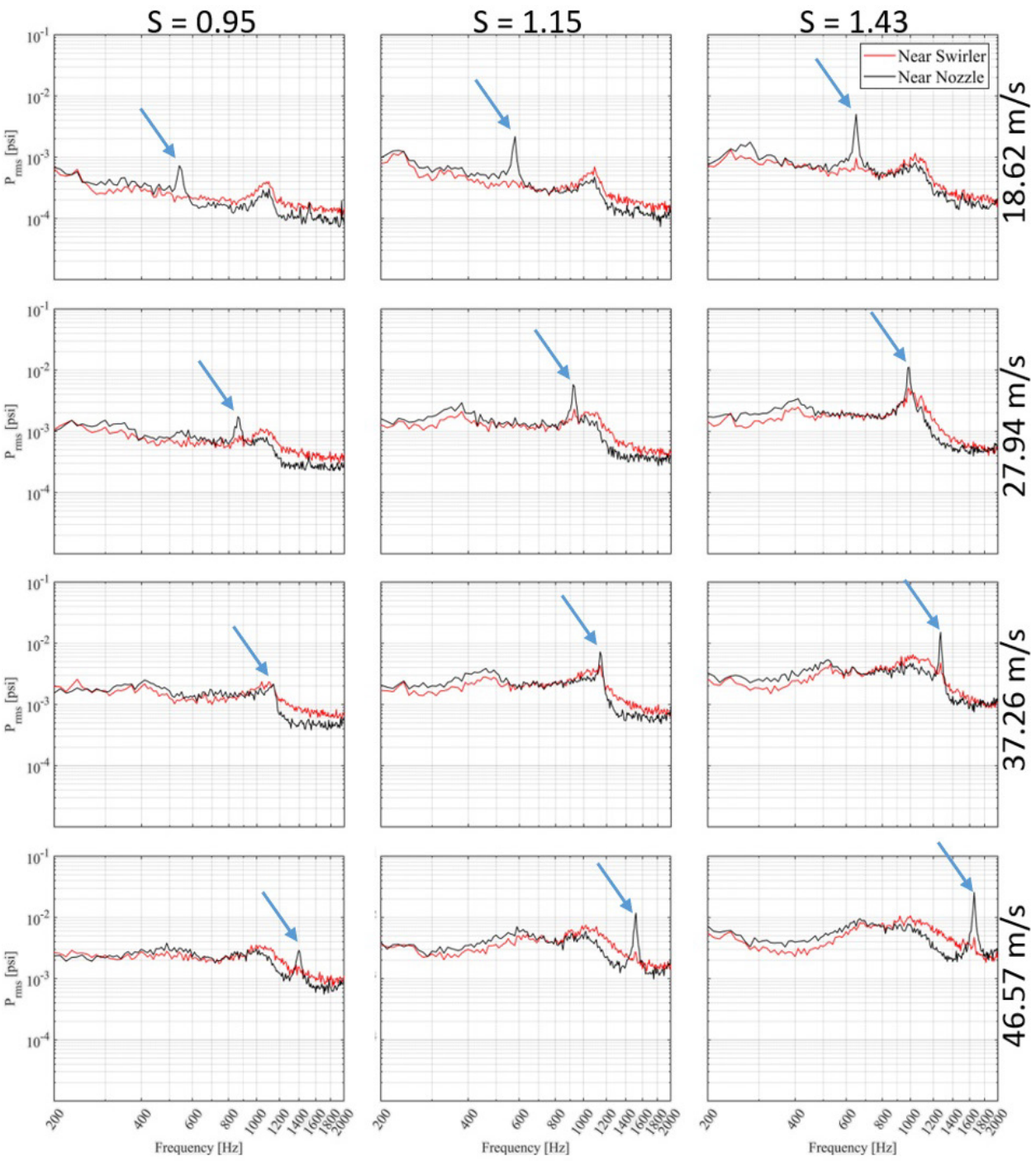

Figure 20: Acoustic response of the PVC at various flow rates and swirl numbers

The frequency response of the PVC operates linearly as a function of bulk flow velocity, $\overline{U}_0$. Figure 21 shows the Strouhal number response of the PVC generated by a flow field at S=1.43 for six different flow rates. The color in the plot represents the magnitude of the response. The Strouhal number non-dimensionalizes frequency by a characteristic length, L, and flow velocity, U.

$$St = \frac{fL}{U}$$

The characteristic length used is the diameter of the nozzle, which is the same for each case. Just like in Figure 20, as the flow rate increases, the amplitude of the PVC increases. However, plotting against Strouhal number demonstrates that all PVCs at a specified swirl number oscillate at the same non-dimensional frequency, which is 0.88 in Figure 21.

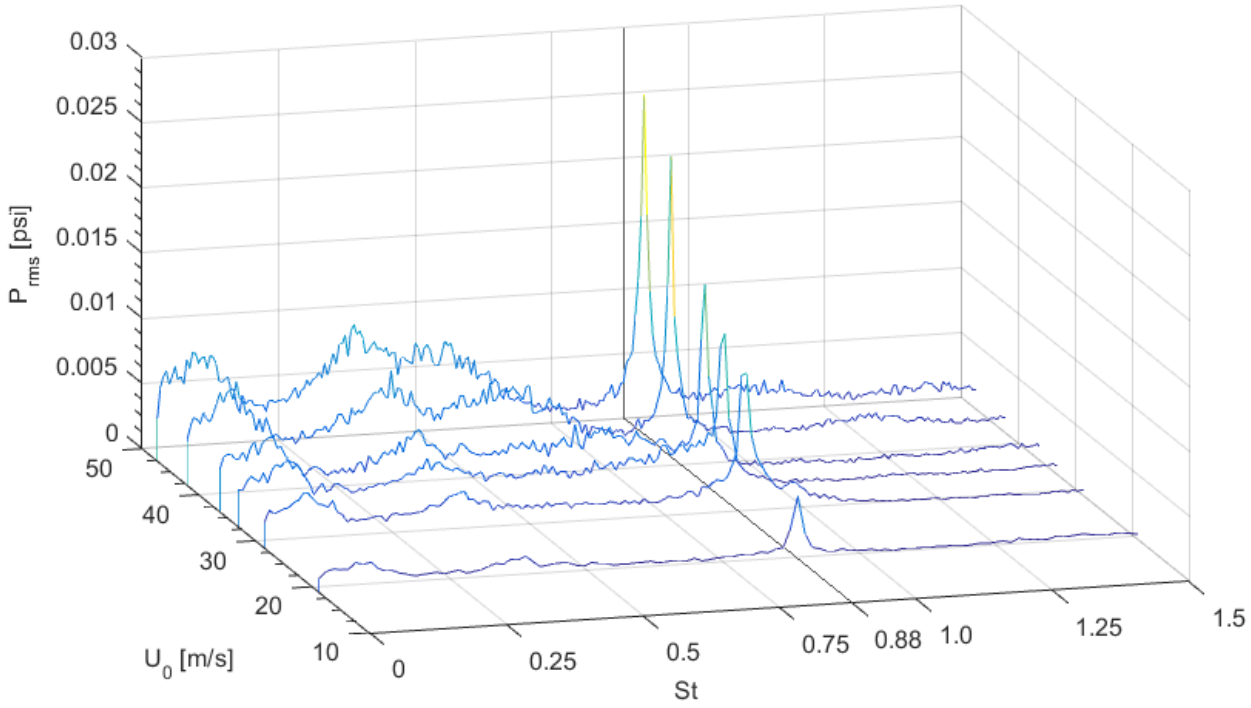

Figure 21: The response of *S*=1.43 swirling flows as a fucntion of Strouhal number and bulk flow velocity

Base Flow Variation with Swirl Number

Seven swirl numbers are studied in this work at various forcing conditions, as shown in Table 1. Forcing will only be explored in Chapter 6. This chapter concerns the listed swirl numbers at unforced conditions. For all cases, the jet is non-reacting, the bulk flow velocity is 28 m/s, the jet is unconfined, and the incoming air is not preheated. In Table 1, VB stands for vortex breakdown.

Table 1: Test matrix with flow state and PVC frequencies

Swirl number	Flow state	PVC frequency	Forcing frequencies
0.00	No VB	—	600 Hz
0.18	No VB	—	600 Hz
0.38	No VB	—	400–700 Hz
0.56	Intermittent VB	—	600 Hz
0.79	Weak PVC	770–815 Hz	600 Hz
1.05	PVC	840 Hz	600 Hz
1.43	Strong PVC	1060 Hz	400–700 Hz

Figure 22 presents the time-averaged flow fields at each swirl number in the *r–x* plane and *r–θ* plane, shown in the top and bottom row, respectively. The horizontal line in each *r–x* image is drawn at *x/D=1.7* and marks the downstream distance of the *r–θ* cuts. The time-averaged streamwise velocity component is shown for the data in the *r–x* plane; the colorbar for the data in the *r–θ* plane is the time-averaged azimuthal velocity. Streamlines are shown on each plot to visualize the direction of the flow.

As swirl number increases, each plane has defining features that illustrate the shift from uniform, non-swirling flow, to VB, and finally to the formation of a PVC. In the *r–x* plane, at *S*=0.00 and 0.18, the flow from the nozzle is uniform and the jet only weakly spreads. This spatially constant behavior is attributed to the lack of swirling motion. As swirl number increases, the streamwise velocity decreases everywhere in the flow. This reduction is due to the momentum of the flow being redistributed from the streamwise direction to the azimuthal direction. At *S*=1.43, the streamwise velocity is approximately 10 m/s less than a case with low swirl. A pocket of negative velocity near the nozzle is indicative of VB and increases in strength as the swirl number increases from 0.79. At high swirl numbers, the streamlines trace a recirculation zone in the center of the jet, which is a defining feature of VB.

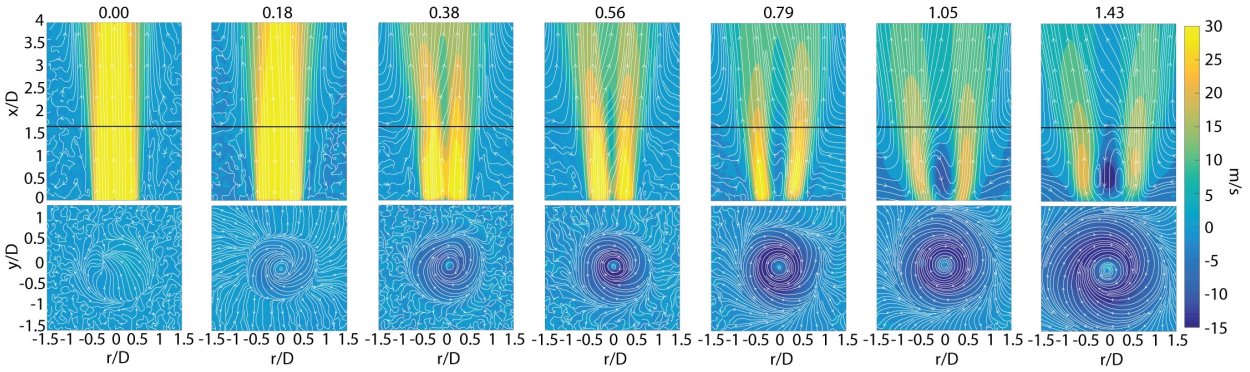

Figure 22: Variation of time-averaged flow field (base flow) with swirl number in *r-x* (top) and *r-θ* (bottom) planes

The plots of the *r–θ* plane also show changes in flow structure as swirl number increases. It is important to note that that reason that azimuthal velocity is negative in these plots is because the swirler is set to negative angles and thus produces a clockwise rotation of the flow. One of the most obvious changes in the *r–θ* plots is the radial extent of the swirling motion, illustrated by the streamlines. At *S*=0.18, a slight swirl is defined and only extends as far as the diameter of the nozzle. Whereas at *S*=1.43, the swirl pattern clearly shows jet spreading. It is also important to note that only unforced cases are presented in Figure 22. But, as shown by Mathews *et al.* [18], the time-averaged flow does not change with forcing, and so these plots are accurate for each swirl number, regardless of forcing.

Self-Excited Dynamics of the Flow

POD is used to illustrate the self-excited dynamics of the flow field as a function of swirl number. Figure 23 shows the strength of modes 1-20 for all swirl numbers. At swirl numbers of 0.79 and above, there exist one or two initial modes with higher energies than the rest, indicating

the presence of self-excited dynamics. It is these high-energy modes that we consider in the analysis of the self-excited dynamics.

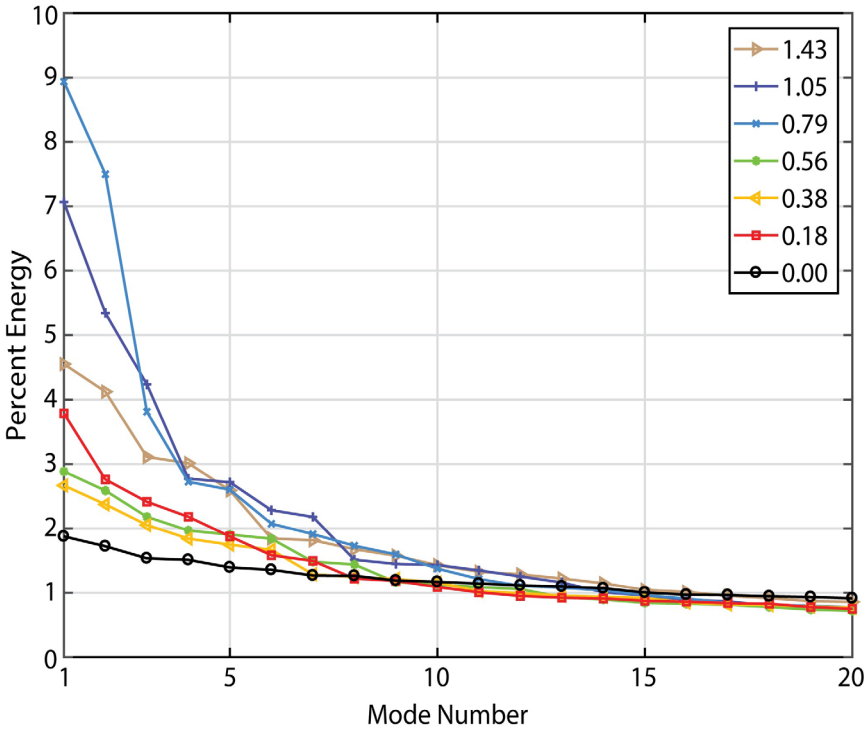

Figure 23: Energies of POD modes 1-20 for all swirl numbers

It is evident from the mode energies that swirl numbers of 0.79 and above contain a PVC. The frequencies of these PVCs were confirmed through acoustic measurements using pressure transducers in the swirler nozzle. Figure 24 shows the reconstructed azimuthal velocity for the POD modes that contain spectral content at the PVC frequency. A reconstruction is performed for three swirl numbers, as shown in the top row of the figure. The second row shows the frequency spectra of mode 1, the highest energy POD mode. The plots in the third row are the pressure spectra at each swirl number. These spectra were obtained using the near-nozzle pressure transducer.

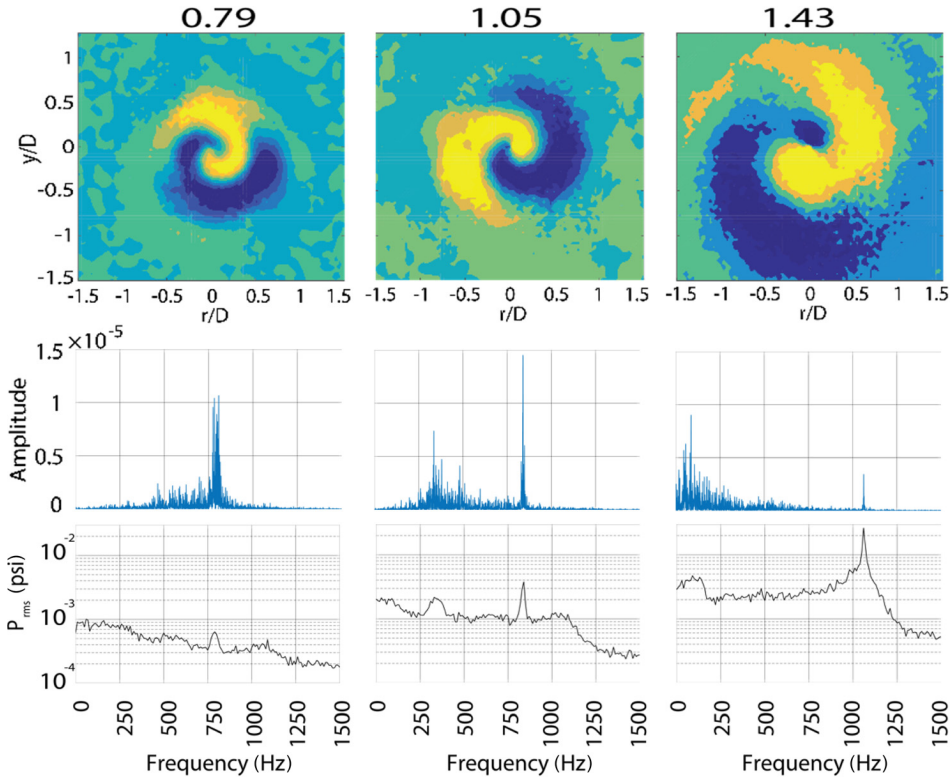

Figure 24: POD reconstruction and frequency spectrum of swirl numbers that cause a PVC to be formed

The reconstructed mode shapes shown in Figure 24 are indicative of a PVC, as the velocity oscillations indicate a helical motion in the flow field. As the swirl number increases, the size of the PVC grows radially as a result of the radially-expanding flow. The spectra of the first POD temporal modes show a defined peak that occurs at the same frequency as the peak obtained using pressure measurements for all three swirl numbers. These peaks occur at the PVC frequency. This is particularly evident for swirl numbers S=1.05 and 1.43, for which the frequency is 840 Hz and 1060 Hz, respectively. At a swirl number of S=0.79, the PVC is noticeably weaker and less coherent. This is evidenced by a broad peak around 800 Hz in POD mode 1 and a bump on the pressure spectra at 800 Hz, which is barely above the noise floor.

O'Connor and Lieuwen showed that the azimuthal dynamics of a PVC can be quantified using an azimuthal decomposition [19]. The azimuthal dynamics can then be compared directly to a linear stability analysis, shown by Hansford *et al.* [22]. Figure 25 shows the results of azimuthal decomposition performed for the cases which contain a PVC, the highest three swirl numbers. The decomposition was performed at the PVC frequency corresponding to its respective swirl number (see Table 1) and at the azimuthal mode numbers *m=1* and *m=-1*. Modes *m=1* and *m=-1* have been shown to be dominant when a PVC is present. Figure 25 plots the mode strength, given as power spectral density of the radial velocity spectrum, as a function of radial distance from the center of the jet. This representation provides a visualization of the spatial extent of the non-axisymmetric modes symptomatic of a PVC.

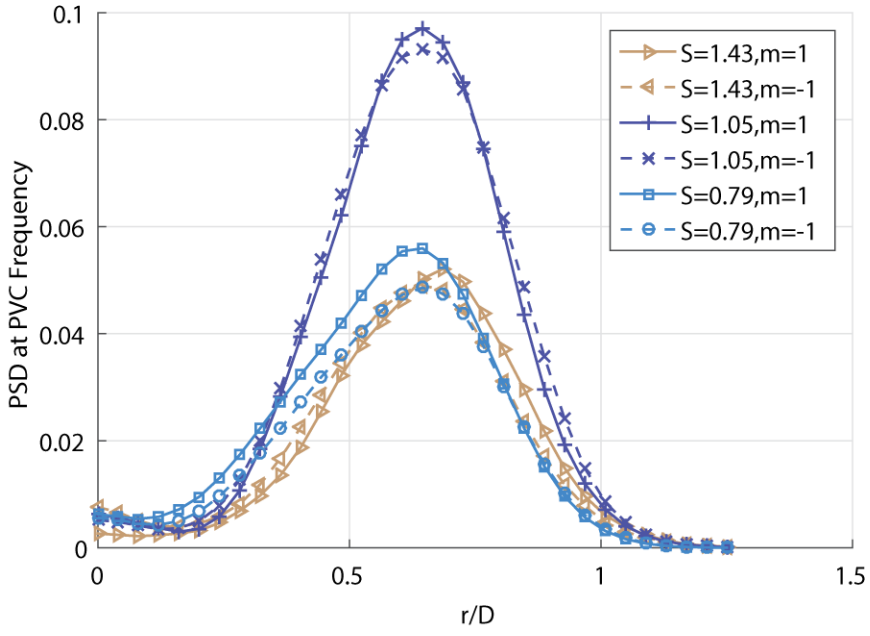

Figure 25: Strength of PVC modes *m=1* and *m=-1* for three swirl number as a function of radius

The radial PVC strength distribution shown in Figure 25 matches up with the PVC mode shapes generated by POD in the top row of Figure 24. The PVC oscillations peak for *S*=0.79 and

S=1.05 at about *r/D=0.7*. For *S*=1.43, the oscillations peak just slightly higher than *r/D=0.7*. The radial location of these peak oscillations aligns with the edge of the POD mode shape for each respective swirl number. The radial location *r/D=0.7* is further significant because it is the location of the shear layer of a swirling flow at *x/D*=1.7. The shear layer is where a PVC manifests.

The mode strength for both non-axisymmetric modes increases as swirl number is increased from *S*=0.79 to *S*=1.05, which is reflected in the POD and pressure measurements as well. The mode strengths for the highest swirl number, *S*=1.43, are lower than those at *S*=1.05, which is a somewhat unexpected result given that the pressure fluctuations from the PVC are significantly stronger at the highest swirl number case. We believe that the reduction in mode strength is the result of a number of factors. Predominantly, as the PVC is extremely strong at this condition, the centrifugal force on the seeding particles is significant and seed is thrown from the center of the flow outwards radially, resulting in lower seeding densities than in the lower-amplitude PVC cases.

Figure 26 presents the azimuthal mode strength as a function of azimuthal mode number. For all three swirl numbers the PVC manifests in both *m=1* and *m=-1* motions. All other modes receive negligible contributions. The lack of response in the *m=0* mode is particularly important because mode *m=0* represents axisymmetric behavior. A PVC is highly non-axisymmetric and precesses around the center of the jet. Therefore, *m=0* motion can be used to identify a forced response because a PVC does not create this motion.

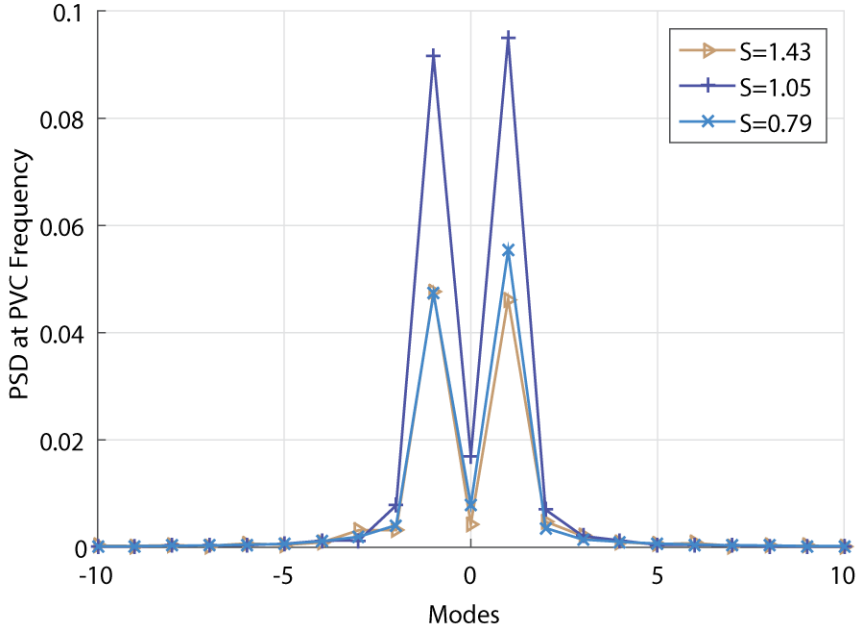

Figure 26: Distribution of modes at the PVC frequency for three swirl numbers and *r/D=0.7*

Chapter 6

Flow Field Response to Acoustic Forcing

PVC Frequency Response to Acoustic Forcing

It is important to determine if the acoustic forcing frequency will have any effect on the amplitude or frequency of the PVC response, so as to understand its role in the combustion instability feedback loop. Figure 27 shows the results of a forcing frequency sweep that is performed while a PVC is present for three flow rates at a swirl number of S=1.43. The PT points show the rig's response to forcing and the 18.62, 27.94, and 46.57 m/s points represent the PVC amplitude response to forcing at the specified flow rates. At 18.62 m/s the PVC exists at 650 Hz, at 27.94 m/s the PVC exists at 950 Hz, and at 46.57 m/s the PVC exists at 1620 Hz. It is clear that forcing at frequencies near the PVC frequency do not change the PVC amplitude.

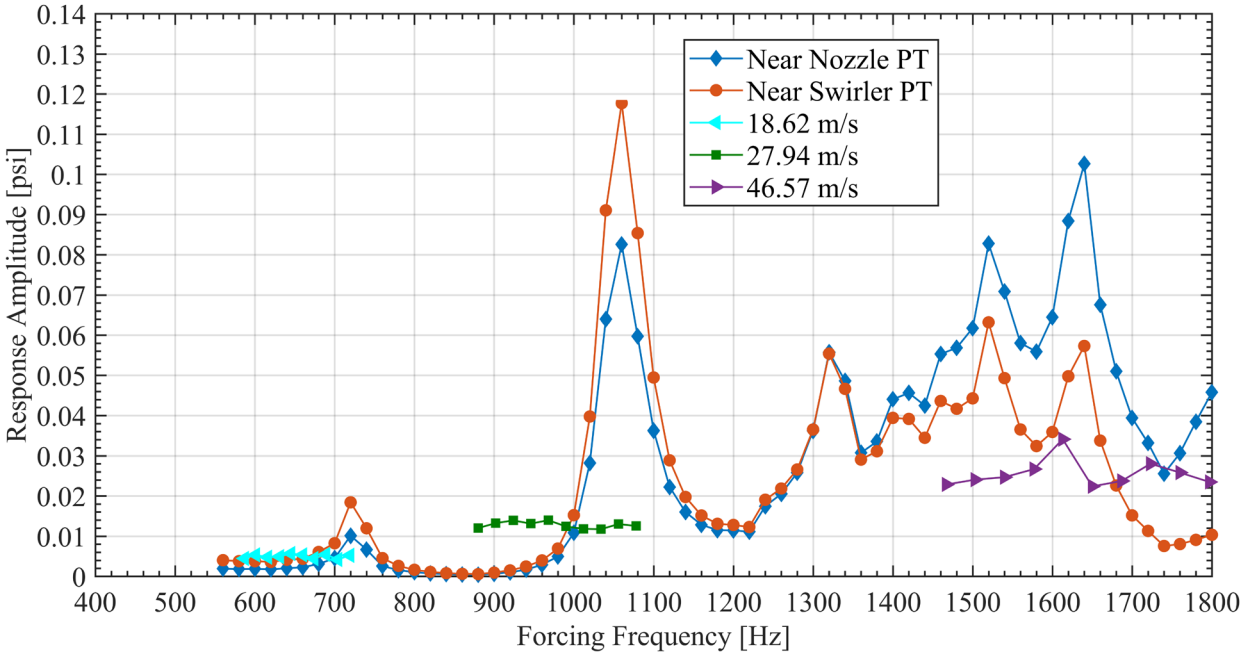

Figure 27: PVC amplitude response to acoustic forcing at various flow rates and S=1.43

Figure 28 explores whether forcing at frequencies near the PVC and at different forcing powers will change the PVC frequency. The results shown are generated at a swirl number of S=0.95 and a flow rate of 46.57 m/s, which produces a PVC at 1440 Hz. The PVC is called out a blue arrow. The flow is forced at two frequencies on either side of the PVC frequency, shown on the right side of the figure, and at three forcing powers, shown along the top row of the figure. In all cases, the PVC frequency remains at 1440 Hz and forcing does not entrain or otherwise alter the PVC frequency. Additionally, and as expected based on the data presented in Figure 27, the PVC amplitude does not change in any of the cases as a result of forcing. The same test was run at both 18.62 m/s and 27.94 m/s and an identical result was observed in each instance. The PVC is "impervious" to the acoustic forcing performed in this study.

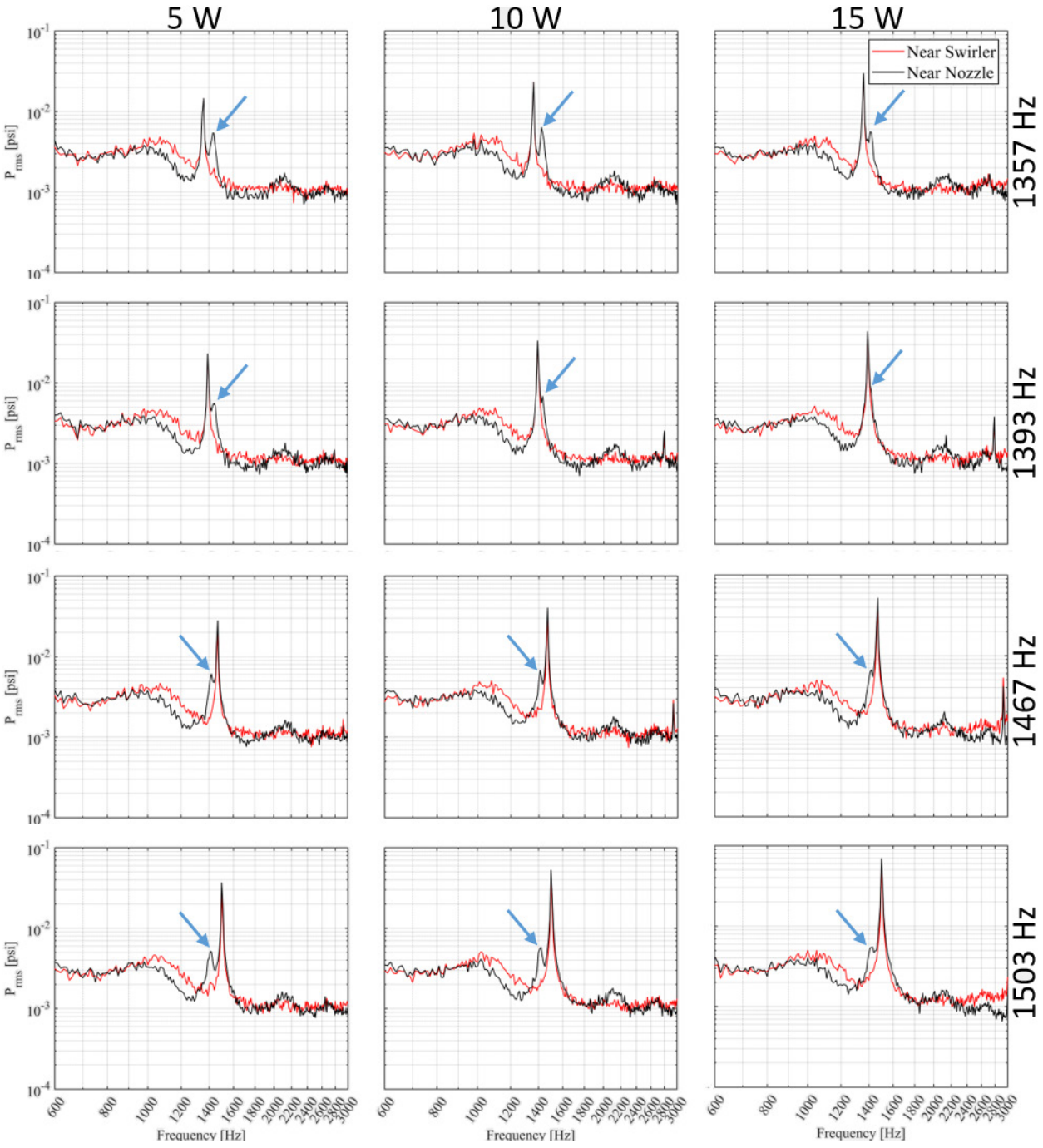

Figure 28: Forcing frequency and amplitude sweep at 46.57 m/s and *S*=0.95

Modal Dynamics of Flow Field Response to Acoustic Forcing

Longitudinal acoustic forcing produces an axisymmetric input disturbance that will manifest as axisymmetric excitation at the base of the flow. This disturbance will convect downstream through the flow. It has already been shown that a PVC produces solely non-axisymmetric flow motion, with negligible axisymmetric components. The difference in modal dynamics produced by these two mechanisms will be used to investigate the relative strength of the acoustic response and self-excited dynamics. Figure 29 presents the azimuthal decomposition of various swirl numbers at mode *m=0* and a frequency of 600 Hz, the forcing frequency (see Table 1). All cases are forced at the same constant amplitude, which is 1% of the mean velocity, defined as $\frac{u_a'}{\bar{u}}$. The data is presented as a function of radial distance from the center of the jet to show the spatial extent of the flow response. The swirl number *S*=0 is not shown because it is difficult to measure radial or azimuthal velocity in a non-swirling jet.

The radial distribution shown in Figure 29 presents three different response regimes. The first of which concerns the low swirl cases of *S*=0.18, 0.38, and 0.56, where no PVC exists. These low swirl cases show a strong response at 600 Hz. The radial location of the peak response amplitude is about *r/D=0.5*, which is the shear layer location of these flows. The second regime is that of a weak response. The only swirl number that falls into this category is *S*=0.79, which shows a response that is much lower than regime one. Here, a weak PVC is present and appears to only be able to dampen the 600 Hz response, not completely suppress it. The third regime contains cases which show no response. Swirl numbers *S*=1.05 and 1.43 fall in this regime and both produce a stable PVC.

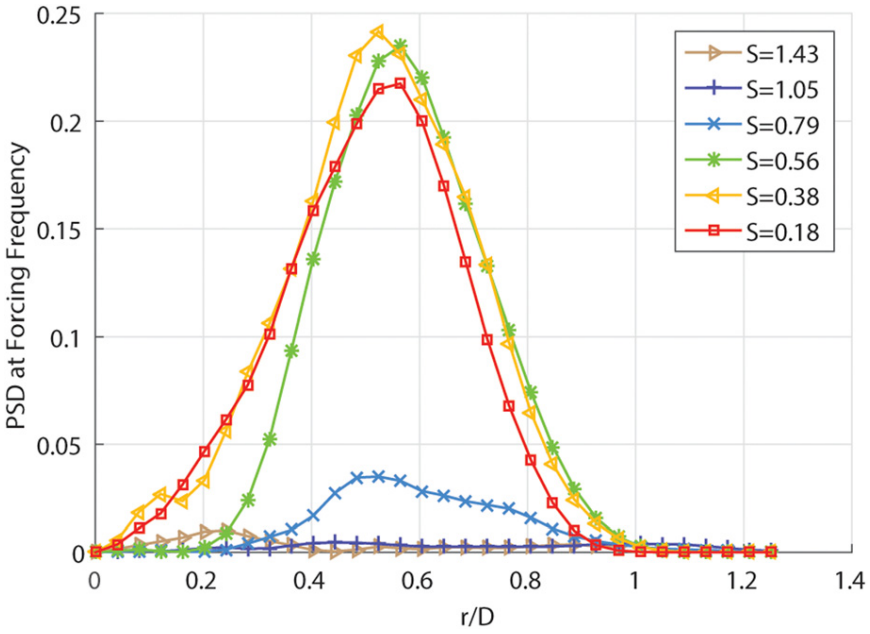

Figure 29: Strength of the *m*=0 mode for a range of swirl numbers at the forcing frequency, 600 Hz

Figure 30(a) presents the modal distribution of the same data shown in Figure 29 at a radial location of *r/D=0.5*. The three lowest swirl numbers, which make up regime one, once again show a very strong mode *m=0* response. These swirl numbers also show very little non-axisymmetric motion, indicating that the flow only responds axisymmetrically to axisymmetric forcing. Linear stability analysis of the flow field at these swirl numbers has shown that these flows do not contain any pockets of absolute instability and are convectively unstable throughout. This stability condition indicates that the flow field is receptive to external forcing, and that the flow will respond not only to the forcing frequency, but also the forcing symmetry. Symmetry-matching response has been shown in studies using transverse acoustic forcing of non-swirling jets, including Kusek *et al.* [23] and Leyva *et al.* [24]. The higher swirl number cases, which all contain PVCs, show no axisymmetric response at the forcing frequency, indicating that the PVC suppresses the forcing response.

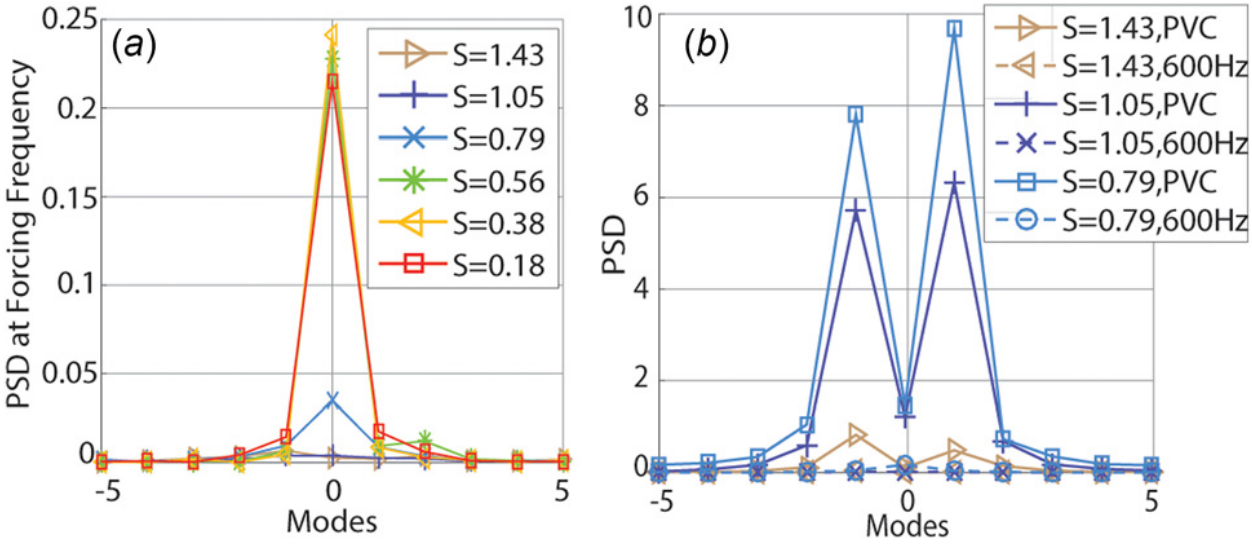

Figure 30: Distribution of modes at 600 Hz for six swirl number and *r/D=0.5* (a) and distribution of modes at 600 Hz and the PVC frequency for the three highest swirl numbers and *r/D=0.5* (b)

Acoustic forcing does not significantly alter the modal distribution of the PVC dynamics in cases that contain a PVC. Figure 30(b) shows the modal distribution of the highest three swirl numbers for an azimuthal decomposition performed at the respective PVC frequency, at 600 Hz forcing, and at a radial location of *r/D=0.5*. The non-axisymmetric modes, *m=1* and *m=-1* are present in the decomposition performed at the PVC frequency, just like with the unforced cases (Figure 26). For *S*=1.43, the response is very low, most likely due to the difficulty in seeding a high swirling flow, but the trend is representative of the true dynamics of the flow field. The modal dynamics of the cases decomposed at the forcing frequency all show a negligible response in all modes, indicative of the PVC suppressing any response.

The reduced forcing response that is seen when a PVC is present, is mirrored at other forcing frequencies as well. Figure 31 shows the radially distributed axisymmetric response of two swirl numbers, *S*=0.38 and 1.43, decomposed at the forcing frequency for a range of forcing frequencies. To avoid the possibility of non-linear coupling with the PVC, the additional forcing

frequencies were chosen so that they do not overlap with the PVC frequency. The swirl number that produces a PVC, S=1.43, shows complete suppression of all axisymmetric motion. The weakly swirling case, S=0.38, shows a clearly axisymmetric response, peaking in the shear layer.

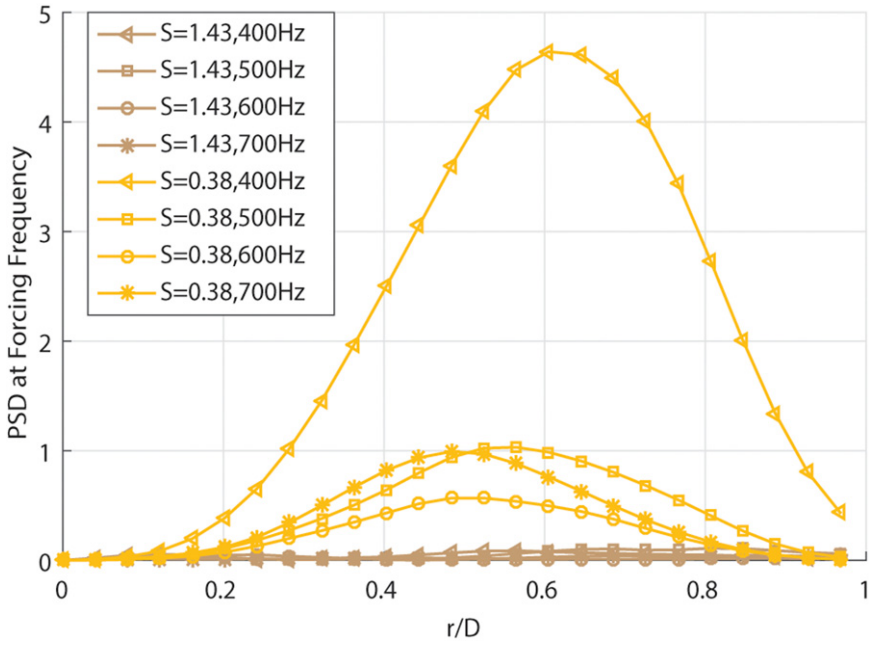

Figure 31: Strength of the m=0 mode for S=0.38 and S=1.43 at a range of forcing frequencies

The m=0 modal response in Figure 31 indicates that the S=0.38 flow field responds to longitudinal acoustic forcing at a range of frequencies. While the response is not the same for all frequencies, there is a coherent, spectrally-narrow response at the forcing frequency, which is mirrored in the POD spectra shown in Figure 32. Here, spectra are shown from both the near-nozzle pressure transducer and the POD; the POD spectra have been scaled to illustrate their content rather than their absolute values. The pressure transducer responds to pressure fluctuations from both acoustic and hydrodynamic sources, and in the acoustically forced cases, the peaks at the forcing frequency are likely to be entirely acoustic content. At S=0.38, the POD,

which is only a reflection of the flow behavior, shows strong, narrow-band response to the acoustic forcing at these frequencies.

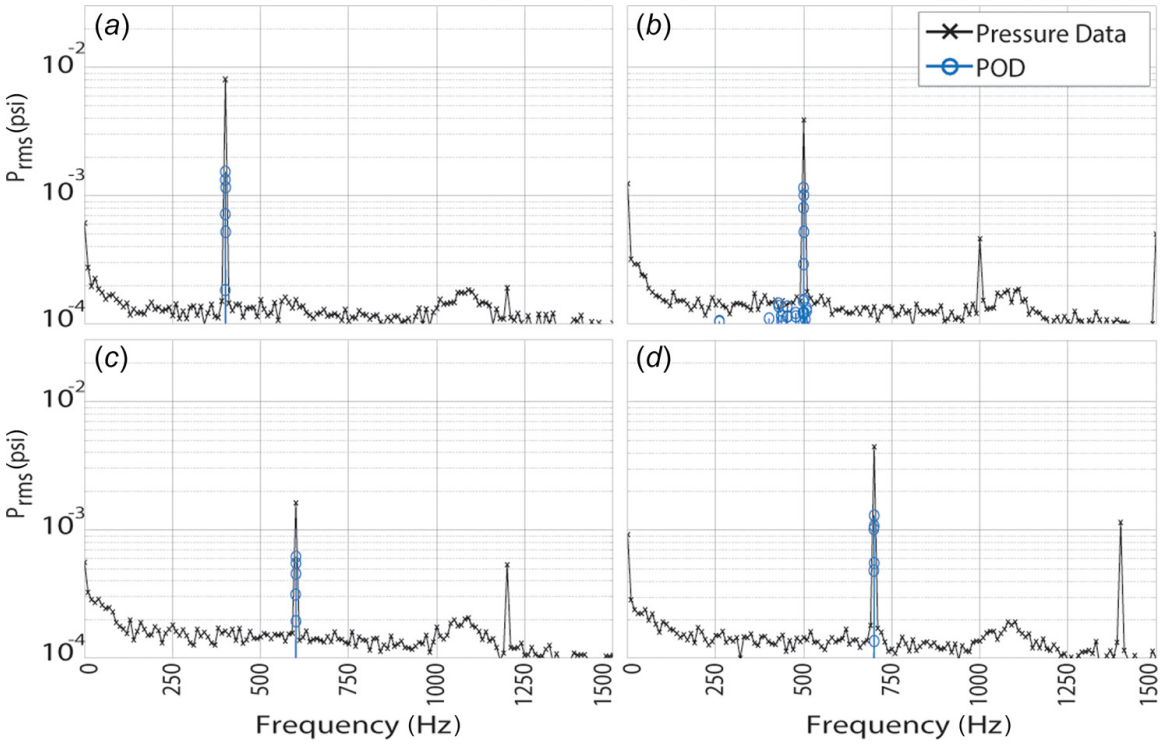

Figure 32: Response of flow at swirl number of *S*=0.38 to acoustic forcing as seen by pressure transducer and POD modes at various forcing frequencies. Forcing at 400 Hz (a), 500 Hz (b), 600 Hz (c), and 700 Hz (d)

At *S*=1.43, the response of the flow field at *m*=0 is equally non-existent at the forcing frequency, as is shown in the radial distribution of mode strengths in Figure 31. This fact is reflected in the pressure and POD spectra shown in Figure 33, where the POD spectra have been scaled to fit on plots with the pressure spectra. In comparing the pressure spectra at *S*=0.38 in Figure 32 and *S*=1.43 in Figure 33, a few interesting points are noticeable. First, the overall sound pressure level is higher at the higher swirl number; this is likely a result of not just the presence of a PVC, but also an increase in flow turbulence, and hence flow noise, that results from the PVC motion. Second, the acoustic forcing frequencies can be seen in the pressure spectra for both cases, and in the *S*=1.43 case, the peak from the PVC is also visible at

approximately 1060 Hz. This peak is matched by a peak in the POD spectrum, which indicates that the source of the pressure oscillations at 1060 Hz is the PVC. However, the POD spectra for *S*=1.43 do not contain significant peaks at the acoustic forcing frequencies, indicating a lack of flow response. The spectrum of each POD mode has been inspected, and no coherent peaks can be found at the forcing frequency in any of the modes for *S*=1.43.

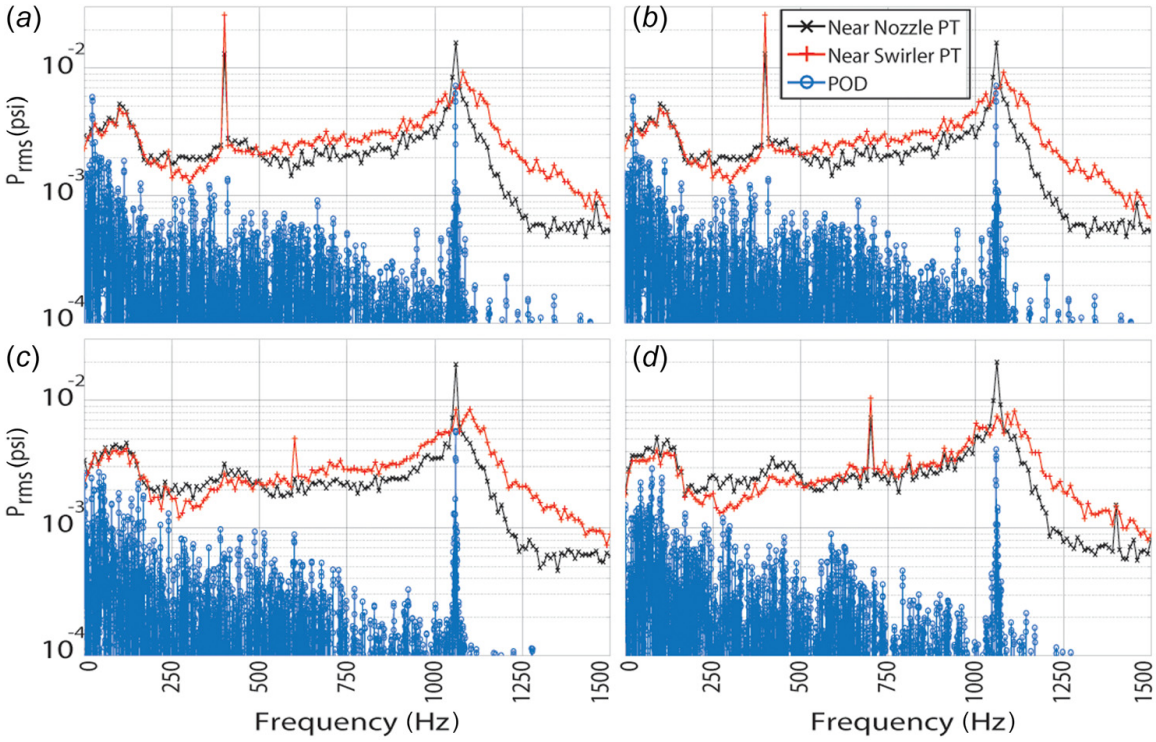

Figure 33: Response of flow at swirl number of *S*=1.43 to acoustic forcing as seen by PT and POD modes at various forcing frequencies. Forcing at 400 Hz (a), 500 Hz (b), 600 Hz (c), and 700 Hz (d)

Response Suppression Mechanism

The preceding experimental results have presented evidence that the shear layer's hydrodynamic response is being suppressed by the PVC. Linear hydrodynamic forced response analysis is used to explain why the PVC suppresses shear layer receptivity. The following

analysis was performed by Dr. Hemchandra on the data collected with this experiment. It proves the experimental hypothesis, that the PVC suppresses the shear layer receptivity of swirling flows.

Figure 34 shows the spatial amplification of the flow's response to 700 Hz acoustic forcing as a function of downstream distance. Swirl numbers $0<S<0.79$, those which do not have a stable PVC, all show a response that exceeds unity downstream of the dump plane. This suggests that at 700 Hz forcing a large axisymmetric response occurs, as seen in the experiment (see Figure 30a). For swirl numbers that produce a stable PVC, S=1.05 and 1.43, the spatial amplification of the axisymmetric response monotonically decreases over downstream distance. This is also consistent with experimental results, which show that there is no mode $m=0$ axisymmetric response to acoustic forcing in cases which contain a PVC.

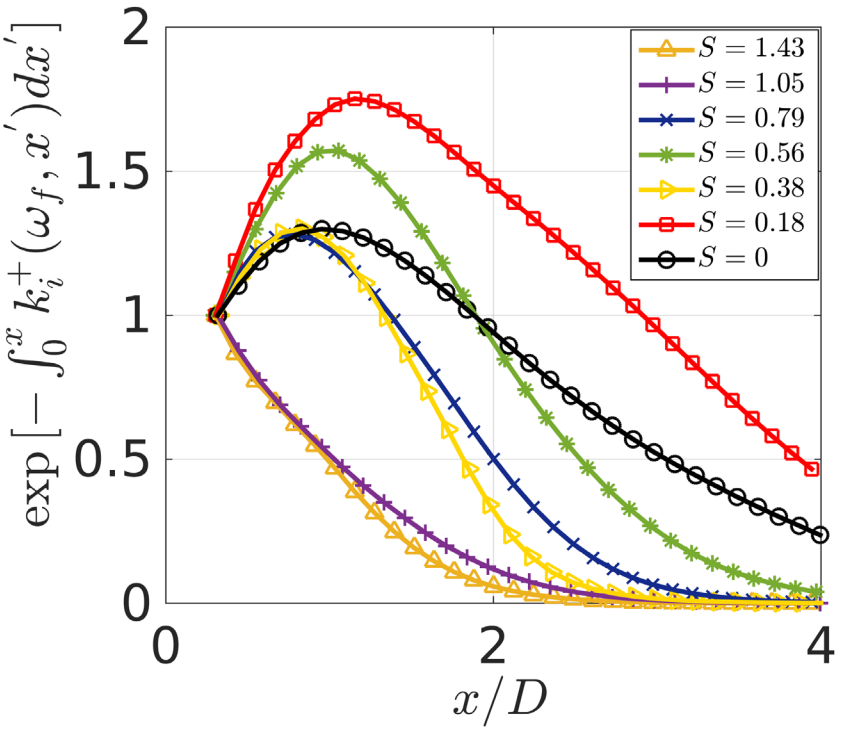

Figure 34: Spatial amplification of flow response to forcing at 700 Hz

Figure 35 shows the variation in the peak values presented in Figure 34 as a function of non-dimensional forcing frequency. f is the forcing frequency, δ_{OSL} is the time-averaged outer shear layer thickness at each swirl number, and U_0 is the axial flow velocity. For 0<S<0.79, the peak spatial amplification exceeds unity for all conditions examined in this study. However, for S=1.05 and 1.43 the peak spatial amplification remains near unity for all forcing frequencies, showing that velocity disturbances will uniformly decay along the streamwise direction for those swirl numbers which produce a PVC.

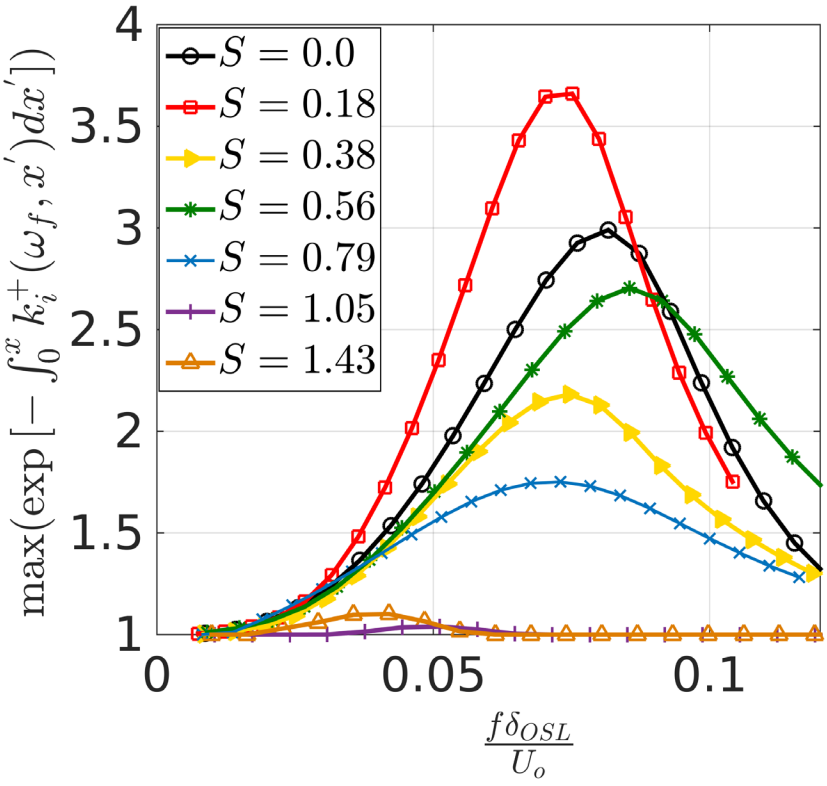

Figure 35: Variation in peak spatial amplification as a function of non-dimensional forcing frequency for various swirl numbers

The reason for the shear layer response suppression is shown in Figure 36, where $\overline{U}_x$ and $\overline{U}_\theta$ are plotted as a function of radial location for various swirl numbers at a downstream distance of *x/D=0.3*. This downstream location is where the local spatial growth rate is maximum across

swirl number. Figure 36a shows the radial profile of $\bar{U}_x$. It is clearly evident that the outer shear layer thickness if significantly larger for S=1.05 and 1.43, where a PVC is present, than for S<0.79. The peak axial velocity is also reduced when a PVC is present. The larger shear layer and lesser velocity would reduce the time-averaged azimuthal vorticity strength across the outer shear layer. The same effect is seen in Figure 36b, where $\bar{U}_\theta$ is plotted. The same trends are seen at other axial locations.

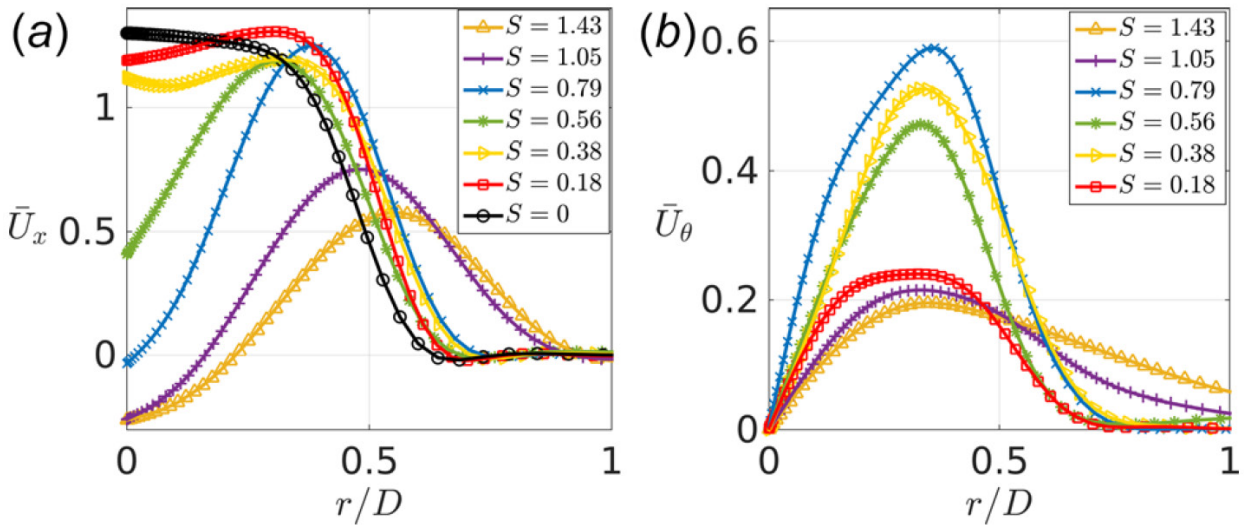

Figure 36: Radial profiles at various swirl numbers, S, of time-averaged base flow velocity components (a) $\bar{U}_x$and (b) $\bar{U}_\theta$, at *x/D=0.3*

Recent location stability analysis [25, 26] has shown that the Kelvin-Helmholtz mechanism is primarily responsible for the growth of fluctuating vorticity production. Thickening of the shear layer results in the progressive weakening of the Kelvin-Helmholtz mechanism. Therefore, when axisymmetric forcing is introduced at S>0.79, the PVC alters the base flow such that the shear layers thicken and significant levels of coherent fluctuating vorticity is not generated. This causes the hydrodynamic response of the forcing to decay spatially.

Chapter 7

Conclusions and Future Work

This work has demonstrated how a precessing vortex core can suppress the receptivity of a swirling flow field to longitudinal acoustic forcing through both experiment and linear stability analysis. Data obtained at a range of swirl numbers are used to quantify the self-excited dynamics of the flow as a function of swirl number. Measurements in the r–θ plane are used to calculate POD modes to understand the structural characteristics of these flows, and azimuthal decompositions of the radial velocity fluctuations are used to quantify the azimuthal behavior of the disturbances. Flow with a PVC displays strong oscillations at modes m=1 and m=-1.

Flow response to acoustic forcing is measured at a range of forcing frequencies, quantifying the response of the flow to the longitudinal forcing using the $m=0$ mode at the forcing frequency as a marker for flow response. Flow fields without a PVC respond to the acoustic forcing through narrow-band shear layer oscillations, while flows with the PVC do not respond at any of the forcing frequencies. Forced response analysis of the base flow shows that these differences in response are driven by the shear layer thicknesses and a weakening of the Kelvin–Helmholtz mechanisms in the flow field.

The results of this study could have significant implications for the suppression of combustion instability in lean-burn, low-NOx gas turbines. Suppression of combustion instability is an important design criterion, and designing a system that is naturally resistant to instability may be both operationally and economically favorable to designing passive and active control mechanisms. There are significant strides in understanding that must be made, though, before this method of instability suppression is robust enough for industrial use.

Follow-on work to the results presented in this study focuses in two directions. First, to further investigate the dynamics of the PVC and how linear stability analysis can be interpreted in the case of very strong PVCs. As linear stability analysis has proved to be a particularly useful tool for understanding both the self-excited behavior and forced response of swirling flows, it is critical that this tool be extended to regimes where nonlinear oscillations are important. Second, it is important to note that a PVC will not universally suppress the response of the flow to external excitation. In some cases, like those described by Steinberg *et al.* [27], the PVC can nonlinearly couple with the acoustically driven motions. Using a combination of linear stability analysis and experiment will allow for an understanding of how this PVC design may be achieved. In this way, PVC as a combustion dynamics suppression methodology may be realizable.

BIBLIOGRAPHY

1. Jacobs, M., *High pressure for low emissions: How civil society created the Paris climate agreement.* Juncture, 2016. **22**(4): p. 314-323.
2. Lieuwen, T.C. and V. Yang, *Gas turbine emissions*, in *Cambridge aerospace series 38*. p. 1 online resource.
3. Zinn, B.T. and T.C. Lieuwen, *Combustion Instabilities: Basic Concepts*, in *Combustion Instabilities in Gas Turbine Engines: Operational Experience, Fundamental Mechanisms, and Modeling*, T.C. Lieuwen and V. Yang, Editors. 2005, AIAA: Reston, VA.
4. Smith, K.O. and J. Blust, *Combustion Instabilities in Industrial Gas Turbines: Solar Turbines' Experience*, in *Combustion Instabilities in Gas Turbine Engines: Operational Experience, Fundamental Mechanisms, and Modeling*, T.C. Lieuwen and V. Yang, Editors. 2005, AIAA: Reston, VA.
5. Cohen, J.M., W. Proscia, and J. DeLaat, *Characterization and Control of Aeroengine Combustion Instability: Pratt & Whitney and NASA Experience*, in *Combustion Instabilities in Gas Turbine Engines: Operational Experience, Fundamental Mechanisms, and Modeling*, T.C. Lieuwen and V. Yang, Editors. 2005, AIAA: Reston, VA.
6. Ducruix, S., Schuller, T., Durox, D., Candel, S., *Combustion Dynamics and Instabilites: Elementary Coupling and Driving Mechanisms.* Journal of Propulsion and Power, 2003. **19**(5): p. 722-734.
7. Lieuwen, T., V. McDonell, E. Petersen, and D. Santavicca, *Fuel flexibility influences on premixed combustor blowout, flashback autoignition and stability.* Journal of Engineering for Gas Turbines and Power-Transactions of the Asme, 2008. **130**(1): p. 011506-011506-10.
8. Lefebvre, A.H., *Gas turbine combustion*. 2nd ed. 1999, Philadelphia: Taylor & Francis. 400 pages.
9. Candel, S., D. Durox, T. Schuller, J.F. Bourgouin, and J.P. Moeck, *Dynamics of Swirling Flames.* Annual Review of Fluid Mechanics, Vol 46, 2014. **46**: p. 147-173.
10. Paschereit, C.O., P. Flohr, and E.J. Gutmark, *Combustion Control by Vortex Breakdown Stabilization.* Journal of Turbomachinery, 2006. **128**(4): p. 679.
11. Liang, H.Z. and T. Maxworthy, *An experimental investigation of swirling jets.* Journal of Fluid Mechanics, 2005. **525**: p. 115-159.
12. Cala, C.E., E.C. Fernandes, M.V. Heitor, and S.I. Shtork, *Coherent structures in unsteady swirling jet flow.* Experiments in Fluids, 2006. **40**(2): p. 267-276.
13. Kuhn, P., J.P. Moeck, C.O. Paschereit, and K. Oberleithner, *Control of the Precessing Vortex Core by Open and Closed-Loop Forcing in the Jet Core.* Proceedings of the Asme Turbo Expo: Turbine Technical Conference and Exposition, 2016, Vol 4b, 2016(49767).
14. Lopez, J.M., Y.D. Cui, F. Marques, and T.T. Lim, *Quenching of vortex breakdown oscillations via harmonic modulation.* Journal of Fluid Mechanics, 2008. **599**: p. 441-464.
15. Syred, N., *A review of oscillation mechanisms and the role of the precessing vortex core (PVC) in swirl combustion systems.* Progress in Energy and Combustion Science, 2006. **32**(2): p. 93-161.

16. Oberleithner, K., M. Sieber, C.N. Nayeri, C.O. Paschereit, C. Petz, H.C. Hege, B.R. Noack, and I. Wygnanski, *Three-dimensional coherent structures in a swirling jet undergoing vortex breakdown: stability analysis and empirical mode construction.* Journal of Fluid Mechanics, 2011. **679**: p. 383-414.
17. Berkooz, G., Holmes, P., Lumley, J.L., *The Propoer Orthogonal Decomposition in the Analysis of Turbulent Flows.* Annual Review of Fluid Mechanics, 1993. **25**: p. 539-575.
18. Mathews, B., S. Hansford, and J. O'Connor, *Impact of Swirling Flow Structure on Shear Layer Vorticity Fluctuation Mechanisms.* Proceedings of the Asme Turbo Expo: Turbine Technical Conference and Exposition, 2016, Vol 4a, 2016(49750).
19. O'Connor, J. and T. Lieuwen, *Recirculation zone dynamics of a transversely excited swirl flow and flame.* Physics of Fluids, 2012. **24**(7): p. 075107.
20. Yang, V. and W.E. Anderson, *Liquid rocket engine combustion instability*. Progress in astronautics and aeronautics. 1995. 575 pages.
21. Ward, K.E., E.N. Jacobs, and R.M. Pinkerton, *The characteristics of 78 related airfoil sections from tests in the variable-density wind tunnel*. 1 electronic document.
22. Hansford, S., O'Connor, J., Manoharan, K., Hemchandra, S., *Impact of Flow Non-Axisymmetry on Swirling Flow Dynamics and Receptivity to Acoustics*, in *Turbo Expo 2015*. 2015: Montreal, Canada.
23. Kusek, S.M., Corke, T.C., Reisenthel,P., *Seeding of helical modes in the initial region of an axisymmetric jet.* Experiments in Fluids, 1990. **10**: p. 116-124.
24. Leyva, I.A., J.I. Roiguez, B. Chehroudi, and D. Talley, *Preliminary Results on Coaxial Jet Spread Angles and the Effects of Variable Phase Transverse Acoustic Fields* in *46th AIAA Aerospace Sciences Meeting and Exhibit*. 2008, AIAA: Reno, Nevada.
25. Manoharan, K., Hansford, S., O'Connor, J., Hemchandra, S., *Instability Mechanism in a Swirl Flow Combustor: Precession of Vortex Core and Influence of Density Gradient*, in *ASME Turbo Expo 2015*, ASME, Editor. 2015: Montreal.
26. Gaillaire, F., Chomaz, J.-M., *Instability Mechanisms in Swirling Flows.* Physics of Fluids, 2003. **15**: p. 2622.
27. Steinberg, A.M., I. Boxx, M. Stohr, C.D. Carter, and W. Meier, *Flow-flame interactions causing acoustically coupled heat release fluctuations in a thermo-acoustically unstable gas turbine model combustor.* Combustion and Flame, 2010. **157**(12): p. 2250-2266.

Academic Vita
Mark D. Frederick

Education

B.S. in Mechanical Engineering **May 2018**
The Pennsylvania State University, Schreyer Honors College *University Park, PA*

B.S. Honors Thesis *(*Adviser: Dr. Jacqueline O'Connor)
Natural Dynamics of a Precessing Vortex Core in Swirling Flows
Understand the onset of a Precessing Vortex Core and its dynamics in a turbulent regime as it relates to flow field stability.

Education Abroad **Jun 2015**
École Centrale de Nantes *Nantes, France*

- Designed and prototyped a passive amplification system for smartphones using CAD programs

Research Experience

Reacting Flow Dynamics Lab **Dec 2015 - Present**
Laboratory of Dr. Jacqueline O'Connor, Penn State University

- Experimentally explore the underlying physics of velocity coupled combustion instability
- Investigate the role of the Precessing Vortex Core on flow field stability in swirling flows
- Utilize high speed laser diagnostics: Particle Image Velocimetry (PIV)
- Analyze data using Proper Orthogonal Decomposition, azimuthal decomposition, and frequency analysis

Publications

Frederick, M., Dudash, J., O'Connor, J., Manoharan, K., Hemchandra, S., and Brubaker, B. "Impact of Precessing Vortex Core Dynamics on Shear Layer Response in a Swirling Jet," *ASME. J. Eng. Gas Turbines Power*. 2018;140(6)

Clees, S., Lewalle, J., **Frederick, M**., and O'Connor, J. "Vortex Core Dynamics in a Swirling Jet Near Vortex Breakdown" *AIAA SciTech Forum 2018.* Kissimmee, FL.

Presentations

Frederick, M. (2017, Aug) "Internship Exit Report and Technical Recommendations" *Pratt & Whitney.*

- Delivered to the Director and Senior Fellows of the Aerothermal Fluids Organization

Frederick, M., Dudash, J., O'Connor, J., Manoharan, K., Hemchandra, S., and Brubaker, B. (2017, Jun). "Impact of PVC Dynamics on Shear Layer Response in a Swirling Jet," *ASME Turbo Expo 2017*. Charlotte, NC.

Frederick, M., O'Connor, J. (2017, Apr). "Impact of PVC Dynamics on Shear Layer Response in a Swirling Jet," *Undergraduate Research Exhibition Poster Presentation,* University Park, PA.

Industry Experience

Pratt & Whitney, Combustor Group **May 2017 – Aug 2017**
Internship: Aerothermal Fluids *East Hartford, CT*

- Analyzed engine data, hardware, and computation models to understand fundamental physics and assisted in combustor design improvements
- Worked on an interdisciplinary team with durability, design, materials, and research engineers

E-Finity Distributed Generation, Micro-Turbine Distributor **May 2014/15 – Aug 2014/15**
Internship *Wayne, PA*

- Developed and maintained a remote monitoring system to alarm and track all OPC data points associated with micro-turbines deployed in the field using the Niagara OPC Server
- Assisted with routine micro-turbine maintenance in the field

Honors, Awards, and Grants

National Science Foundation, Graduate Research Fellowship Program Awardee **2018 - Present**

Pennsylvania Space Grant Consortium Undergraduate Scholarship **2017-2018**

- Recognizes outstanding undergraduates with a demonstrated potential for graduate study

Schreyer Honors College Scholar Involvement Award **2017**

- Recognizes a senior scholar who demonstrates exceptional leadership and dedication to the college

Thomas Briggs Hunter Memorial Award for Student Leadership in Mechanical Engineering **2017**

- For outstanding qualities of leadership, volunteer spirit, and citizenship to the department, college, or university

Erickson Discovery Grant for Undergraduate Research 2016
Schreyer International Travel Grant 2015
President's Freshman Award 2015
Provost Award 2014-2017
Academic Excellence Scholarship 2014-2017

Leadership & Service

President, Schreyer Honors College Student Council **Aug 2016 (Member, 2014) – May 2017**

- Lead an executive board of 15 members to create opportunities for 70+ members of the Student Council
- Represent the Honors College to the university administration and student government

Service Chair Aug 2015 – May 2016

- Lead the Service Committee to organize and provide service events for the Honors College

Discovery Space of Central Pennsylvania **Nov 2017 – Present**
Floor Exhibit Volunteer *State College, PA*

- Facilitate interactions between parents, children, and the exhibits to promote science education in the community

Search Committee, Dean of The Schreyer Honors College **Oct 2016 – Feb 2017**

- At the request of the Vice President of Academic Affairs, conducted national search for nominees, evaluated application materials, and interviewed candidates

Search Committee, Associate Dean of The Schreyer Honors College **Jul 2016 – Sep 2017**

Student Interviewer, Assistant VP for Undergraduate Education **Aug 2016**

Scholar Advancement Team **Aug 2015 – Present**

- Provide information and tours to donors, special guests, and alumni of the Schreyer Honors College

Teaching Experience

Speaking and Writing Communication Teaching Assistant **Aug 2017- Present**
Department of Mechanical Engineering, Penn State University

- Teach effective technical presentation skills to junior engineering design students
- Conduct large group lessons as well as work individually with students

Professional Affiliations

American Society of Mechanical Engineers (ASME) **Jun 2017- Present**
Student Member

American Institute of Aeronautics and Astronautics (AIAA) **Jun 2017- Present**
Student Member

Activities

Hack PSU, 24-hour Coding Competition **Apr 2016**
Safe Streets

- Won 3rd place out of 46 teams by creating a breathalyzer that interfaces with a user's phone to keep them safe
- Used LabView, an Arduino, and Android Studio to create an app that would disable the user's vehicle and automatically notify friends of the user's location if the user became intoxicated